PHYSICAL REVIEW B **79**, 235401 (2009)

Noise in frequency-modulation dynamic force microscopy

Jérôme Polesel-Maris
CEA Saclay, DSM/IRAMIS/SPCSI, Bat. 462, F-91191 Gif-sur-Yvette, France

Miguel Angel Venegas de la Cerda, David Martrou, and Sébastien Gauthier*
Centre d'Elaboration des Matériaux et d'Etudes Structurales, CNRS, P.O. Box 94347, 29 rue J. Marvig, F-31055 Toulouse, France
(Received 8 January 2009; revised manuscript received 7 May 2009; published 1 June 2009)

Analytical expressions for the noise affecting the different signals of interest in frequency-modulation dynamic force microscopy are derived. Two noise sources are considered, the thermomechanical noise of the cantilever and the noise of the deflection sensor. It is shown that distinguishing between amplitude and phase noise is crucial for a good understanding of the instrument. When the tip is far from the sample surface, in the absence of any tip-substrate interaction, the system reduces to two *independent* feedback loops, the first one maintaining the amplitude at a set point value and the other one keeping a constant phase lag between the tip oscillation and the cantilever excitation force. Closer to the surface, in the presence of tip-substrate interaction, these two loops become coupled to an extent that is determined by the nonlinear character of the cantilever oscillation induced by this interaction. The approximations introduced in deriving these analytical expressions are validated by numerical simulations and a comparison with experimental measurements is proposed. This modeling of the noise in frequency-modulation dynamic force microscopy allows us to derive most of the previously published results in a clear and unified framework. In addition, it demonstrates that the oscillator nonlinearities play an essential role in determining the noise level of the instrument, an effect that was not considered before.

DOI: 10.1103/PhysRevB.79.235401 PACS number(s): 07.79.Lh, 68.37.−d, 46.40.Ff, 05.45.−a

I. INTRODUCTION

Frequency modulation dynamic force microscopy (FM-DFM), also called noncontact atomic force microscopy (NC-AFM), is now well established as a tool to image insulating surfaces with atomic resolution.[1] Initially restricted to vacuum environment, this technique has recently been adapted to ambient and even liquid environment with great success.[2] This evolution was made possible due to many improvements of the instrument itself as well as in the associated experimental methods.

Improving the sensitivity or more precisely the signal-to-noise ratio of the instrument constitutes a major objective in these developments. But to progress in this direction it is necessary to understand what are the important sources of noise and how these noises propagate in the instrument and its control system. Noise in FM-DFM was analyzed by several authors.[3–7] The principal sources of noise have been identified and the limits they set to the measurements have been evaluated,[3,8,9] but the role played by the complex control system at work in FM-DFM has not been considered in details.

The analysis of oscillators affected by both thermal and nonthermal noise sources is a topic of current interest. One of the main objectives in this area is to find ways to reduce the noise of these devices for different applications, for instance, to improve the sensitivity of gravitational wave detectors[10] or to access the quantum regime of an oscillator.[11] The present work is different: it explores the way given noises affect the behavior of the FM-DFM setup but does not consider how these noises could be reduced even if the analysis delivered here could be used as a starting point for that purpose.

In the following, we derive analytical expressions that describe how the different signals of interest are affected by noise for a typical FM-DFM setup. Two noise sources are included, the thermal noise of the cantilever and the intrinsic noise of the deflection sensor. Three cases of increasing complexity are worked out.

First, no tip-surface interaction is considered. Two closed loops are operating to stabilize the cantilever oscillation at its resonance frequency.[4] The first one maintains the amplitude of the cantilever oscillation at a set point value by adjusting the cantilever excitation force; this force provides a measure of the intrinsic energy *dissipation* during the cantilever oscillation.[12] The other one keeps the phase shift between the excitation force of the cantilever and its oscillation at a constant value. After that, an interaction described as the sum of a van der Waals and a Morse contributions is introduced but with a fixed tip-substrate distance. Finally, a distance control feedback loop is added to the system in order to maintain at a constant preset value the shift in the cantilever resonance frequency under the influence of the tip-substrate interaction.

A rigorous analytical treatment of this system is quite difficult due to intrinsic nonlinearities in the control system and in the tip-substrate interaction.[13] Deriving tractable analytical expressions requires some approximations, which are validated in each case by comparison with the results of numerical simulations carried out using a modified MATLAB/SIMULINK[14] version of our virtual AFM.[15,16]

After a general introduction to FM-DFM in Sec. II, we discuss in Sec. III the nature of noise in oscillators, carefully establishing the distinction between amplitude noise and phase noise, which will prove essential for the following developments. The way the cantilever oscillation signal is amplitude and phase-demodulated is analyzed in Secs. IV

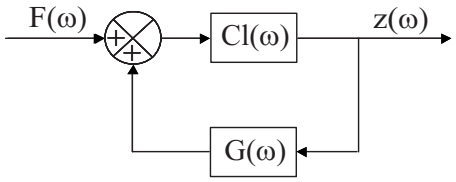

FIG. 1. The cantilever and its positive feedback amplifier G, represented by their harmonic transfer functions $Cl(\omega)$ and $G(\omega)$.

and V. Analytical expressions for the noise perturbing the dissipation and the frequency shift signals are then established in Sec. VI in the situation where the tip is far from the surface. These expressions are compared to the results of numerical simulations in Sec. VII. The tip-substrate interaction is introduced, first maintaining constant the tip-substrate distance in Sec. VIII, then relaxing this constraint in Sec. IX. Section X is devoted to a short comparison of these predictions with experimental measurements. Finally, these results are discussed and a conclusion is given in Sec. XI. Calculation details are presented in Appendixes A–C. A short version of this work was already published.[7]

II. FM-DFM AS A PHASE-CONTROLLED OSCILLATOR

A. Cantilever as a linear oscillator

The cantilever is modeled as a 1 degree-of-freedom dissipative harmonic oscillator,

$$m\ddot{z} = -kz - \gamma\dot{z} + F(t),$$

where $F(t)$ is an external force. k and m are the spring constant and the effective mass of the cantilever. The free resonance frequency is given by $\omega_0 = \sqrt{\frac{k}{m}}$ and the viscosity factor is given by $\gamma = \frac{m\omega_0}{Q}$, where Q is the quality factor of the cantilever. The corresponding harmonic function is given by

$$Cl(\omega) = \frac{z(\omega)}{F(\omega)} = \frac{1}{k\left(\frac{\omega_0^2 - \omega^2}{\omega_0^2} + \frac{j\omega}{Q\omega_0}\right)}, \tag{1}$$

with $F(\omega) = F_0 \exp(j\omega t)$ and $z(\omega) = z_0 \exp(j\omega t)$. Near the positive resonance frequency, $\omega = \omega_0 + \Omega$, with $\Omega \ll \omega_0$,

$$Cl(\omega_0 + \Omega) = C(\Omega) \simeq \frac{1}{k\left(-\frac{2\Omega}{\omega_0} + \frac{j}{Q}\right)} = -j\frac{Q}{k}\frac{1}{(1 + j\Omega\tau_c)}, \tag{2}$$

where $\tau_c = \frac{2Q}{\omega_0}$. The cantilever behaves as a first order low-pass (LP) filter for the frequency detuning $\Omega = \omega - \omega_0$ in the vicinity of the resonance.

B. Phase-controlled oscillator

FM-DFM is based on a phase-controlled oscillator[4] whose the cantilever is the frequency determining element (Fig. 1). The closed-loop transfer function of the system is

$$T(\omega) = \frac{z(\omega)}{F(\omega)} = \frac{Cl(\omega)}{1 - Cl(\omega)G(\omega)}.$$

Oscillations at frequency ω_c are obtained if $1 - Cl(\omega_c)G(\omega_c) = 0$, that is, if

$$|Cl(\omega_c)||G(\omega_c)| = 1,$$

$$\Phi_{Cl}(\omega_c) + \Phi_G(\omega_c) = 0,$$

where Φ_{Cl} and Φ_G are the arguments of $Cl(\omega)$ and $G(\omega)$. Using the second condition and expression (1), one obtains

$$\Phi_G(\omega_c) - \arctan\left[\frac{\omega_c}{Q\omega_0}\frac{1}{1 - \frac{\omega_c^2}{\omega_0^2}}\right] = 0 \tag{3}$$

and

$$\omega_c = -\frac{\omega_0}{2Q\tan[\Phi_G(\omega_c)]} + \omega_0\sqrt{\frac{1}{4Q^2\tan^2[\Phi_G(\omega_c)]} + 1}. \tag{4}$$

This expression shows how the phase setting of the feedback amplifier $G(\omega)$ controls the oscillator frequency ω_c. In general, this frequency will be different from ω_0, the free resonant frequency of the cantilever. In this situation, a change in the Q factor due to a dissipative tip-substrate interaction will induce a shift of the oscillation frequency. This undesirable coupling can be avoided only if $\omega_c = \omega_0$. Then,

$$|G(\omega_0)| = \frac{1}{|Cl(\omega_0)|} = \frac{k}{Q}, \tag{5}$$

$$\Phi_G(\omega_0) = -\Phi_{Cl}(\omega_0) = \frac{\pi}{2}. \tag{6}$$

In the following, we will consider that these relations are always satisfied. Note however that, at least for high Q cantilevers, this coupling is very weak and the instrument is quite robust with respect to phase detuning.[17]

Figure 2 shows how this oscillator is implemented in FM-DFM. Two feedback loops are necessary: the first one uses an automatic gain control (AGC) circuit to keep the amplitude at a constant level A_{sp} defined by the user, satisfying condition (5). The second one maintains the optimal phase relationship given by condition (6) by means of a phase-locked loop (PLL) circuit including a phase shifter. The role of this circuit is not only to generate a sinusoidal waveform at the frequency detected at its input but also to measure the frequency shift $\Delta f(t)$. First FM-DFM systems used an analog quadrature frequency demodulator based on passive components.[3] Today, PLL systems are present in most FM-DFM due to their higher stability and signal-to-noise ratio.[19]

Before analyzing the noise of this oscillator, it is useful to discuss the nature of noise in oscillators and the way the AGC and the PLL transform different types of noise.

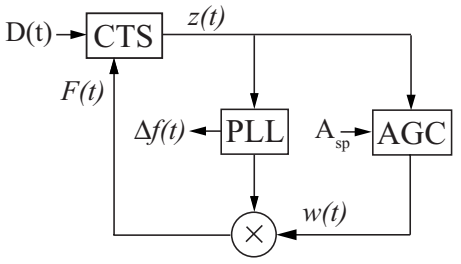

FIG. 2. The two feedback loops necessary to keep the oscillating cantilever at its resonance frequency with a constant amplitude $A_c = A_{sp}$, where A_{sp} is the amplitude set point. CTS represents the cantilever-tip-substrate system with two inputs: the excitation force $F(t)$ and the cantilever-substrate distance $D(t)$. The output $z(t)$ is the oscillation of the cantilever measured by a deflection sensor such as a two-quadrant photodiode in the case of the optical beam deflection method (Ref. 18). The automatic distance control (ADC) feedback loop, which uses the signal $\Delta f(t)$ to control the distance $D(t)$, is not included in the figure.

III. NOISE IN OSCILLATORS

A. Sinusoidal representation of narrow band noise

The minimal coherence time of a signal at the output of a band-pass filter of width $\Delta\omega$ scales as $\Delta\omega^{-1}$.[20] The reason is that the time needed to build a significant phase difference $\Delta\varphi$ between two sinusoidal components at $\omega_c - \frac{\Delta\omega}{2}$ and $\omega_c + \frac{\Delta\omega}{2}$, where ω_c stands for the central frequency of the filter, is given by $\Delta t = \frac{\Delta\varphi}{\Delta\omega}$. The high Q cantilevers used in FM-DFM behave as narrow band-pass filters of coherence time $\tau_c = \frac{2Q}{\omega_c}$ as indicated by expression (2). τ_c is in general 1 order of magnitude greater than the time response of the electronics. In these conditions, the time taken by a signal to travel around one of the feedback loops of the control system is negligible compared to τ_c; the signal remains coherent and noise can be safely considered as a superposition of independent perfect sinusoidal components.

Noises will be characterized by their power spectral density (PSD). Errors and confusions are reproduced in many papers due to implicit conventions concerning spectral analysis. Here we consider positive and negative frequencies, implying that, unless otherwise stated, we consider *two-sided* PSDs. To get *one-sided* PSDs, the displayed spectra should be multiplied by two and considered only in the positive frequency domain.

In the following analysis, a noise $x(t)$ of PSD $S_x(\Omega)$ will be represented by a sinusoidal component $x_s(t) = x_0 \sin(\Omega t)$. x_0 is related to $S_x(\Omega)$, expressed in (dimension of $x)^2$ Hz^{-1}, by the following relation:

$$S_x(\Omega) \times 1 \text{ Hz} = \left(\frac{x_0}{2}\right)^2,$$

obtained by equating the mean square value of the noise $x(t)$ in a 1 Hz bandwidth to the mean square value of $x_s(t)$.[20]

B. Amplitude noise and phase noise

Amplitude and phase noise (PN) refer to a *carrier* signal

$$a(t) = A_c \sin(\omega_c t + \theta_c), \tag{7}$$

with A_c, ω_c, and θ_c being the amplitude, the frequency, and the phase of the carrier. In the following, $\theta_c = 0$, with no loss of generality.

1. Amplitude noise

Amplitude noise modulates the amplitude A_c of the carrier,

$$a(t) = A_c[1 + m(t)]\sin(\omega_c t). \tag{8}$$

As discussed in the preceding paragraph and following Robins[20] and Cleland and Roukes,[21] we represent the amplitude noise by a single sinusoidal component $m(t) = m_0 \cos(\Omega t + \theta_a)$. Then,

$$a(t) = A_c \sin(\omega_c t) + A_c \frac{m_0}{2} \sin[(\omega_c + \Omega)t + \theta_a]$$

$$+ A_c \frac{m_0}{2} \sin[(\omega_c - \Omega)t - \theta_a]. \tag{9}$$

The amplitude modulation generates *sidebands* at $\pm\Omega$ from the carrier, with amplitude $A_c \frac{m_0}{2}$. The lower sideband is *phase coherent* with the upper sideband with the *same* sign. This is the signature of *amplitude noise*.

2. Phase noise

Phase noise modulates the phase of the carrier,

$$a(t) = A_c \sin[\omega_c t + \phi(t)]. \tag{10}$$

Here too, we consider a single phase noise component $\phi(t) = \phi_0 \sin(\Omega t + \theta_\phi)$ with $\phi_0 \ll 2\pi$. Then,

$$a(t) = A_c \sin(\omega_c t) + A_c \frac{\phi_0}{2} \sin[(\omega_c + \Omega)t + \theta_\phi]$$

$$- A_c \frac{\phi_0}{2} \sin[(\omega_c - \Omega)t - \theta_\phi] + \mathcal{O}(\phi_0^2). \tag{11}$$

The phase modulation generates sidebands at $\pm\Omega$ from the carrier, with amplitude $A_c \frac{\phi_0}{2}$. The lower sideband is phase coherent with the upper sideband with the *opposite* sign. This is the signature of *phase noise*.

Frequency modulation is related to phase modulation by

$$\omega(t) = \frac{d[\omega_c t + \phi(t)]}{dt} = \omega_c + \frac{d\phi(t)}{dt}.$$

Hence, one obtains the time dependent frequency variation,

$$\Delta f(t) = \frac{\omega(t) - \omega_c}{2\pi} = \frac{1}{2\pi}\frac{d\phi(t)}{dt} = \frac{\Omega}{2\pi}\phi_0 \cos(\Omega t + \theta_\phi).$$

3. Combination of amplitude and phase noises

These expressions are easily generalized to the case of amplitude *and* phase modulated carrier,

$$a(t) = A_c[1 + m(t)]\sin[\omega_c t + \phi(t)], \tag{12}$$

giving

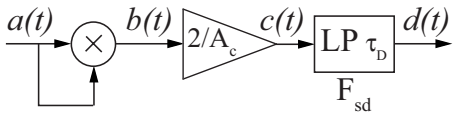

FIG. 3. Block scheme of the synchronous demodulator.

$$a(t) = A_c \sin(\omega_c t) + A_c \frac{m_0}{2}\{\sin[(\omega_c + \Omega)t + \theta_a] + \sin[(\omega_c - \Omega)t - \theta_a]\} + A_c \frac{\phi_0}{2}\{\sin[(\omega_c + \Omega)t + \theta_\phi] - \sin[(\omega_c - \Omega)t - \theta_\phi]\} + \mathcal{O}(m_0\phi_0, \phi_0^2). \quad (13)$$

Expressions (12) and (13) are equivalent ways of expressing the same noise.

IV. AMPLITUDE DEMODULATION: THE SYNCHRONOUS DEMODULATOR

The function of an amplitude demodulator is to extract the amplitude A_c from a modulated waveform as represented by expressions (12) and (13). We discuss here the case of a synchronous demodulator (SD). This device is critical in the analysis of our model FM-DFM setup because it includes a multiplier, which is considered as a nonlinear element in control theory.[22] Several ways exist to model this element.[23–25] We propose the scheme shown in Fig. 3 where the signal is first multiplied by itself, then passed through the first-order LP filter.

If we apply the signal given by Eq. (13) at the input, with $m_0 \ll 1$ and $\phi_0 \ll 2\pi$, we obtain (see Fig. 3 for the labeling of the signals)

$$\begin{aligned} b(t) &= a^2(t) \\ &\approx A_c^2 \sin^2(\omega_c t) + A_c^2 m_0 \sin(\omega_c t)\sin[(\omega_c + \Omega)t + \theta_a] \\ &\quad + A_c^2 m_0 \sin(\omega_c t)\sin[(\omega_c - \Omega)t - \theta_a] \\ &\quad + A_c^2 \phi_0 \sin(\omega_c t)\sin[(\omega_c + \Omega)t + \theta_\phi] \\ &\quad - A_c^2 \phi_0 \sin(\omega_c t)\sin[(\omega_c - \Omega)t - \theta_\phi], \end{aligned}$$

where second-order noise contributions (involving the products m_0^2, $m_0\phi_0$, or ϕ_0^2) are neglected. Ignoring the high frequency components at $2\omega_c \pm \Omega$ ($\Omega \ll \omega_c$), which will be eliminated by the LP filter, we get, after the $2/A_c$ gain,

$$c(t) = A_c + 2A_c m_0 \cos(\Omega t + \theta_a)$$

and finally after LP

$$d(t) = F_{\rm sd}(0)A_c + A_c m_0\{F_{\rm sd}(\Omega)\exp[j(\Omega t + \theta_a)] + \overline{F_{\rm sd}(\Omega)}\exp[-j(\Omega t + \theta_a)]\}, \quad (14)$$

where

$$F_{\rm sd}(\Omega) = \frac{1}{1 + j\Omega\tau_D} \quad (15)$$

is the harmonic function of the low-pass filter and $\overline{F_{\rm sd}(\Omega)}$ stands for its complex conjugate.

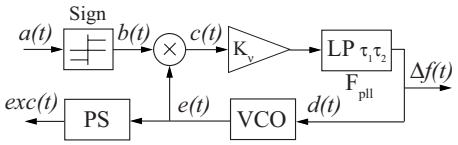

FIG. 4. Block diagram of the PLL. VCO: voltage controlled oscillator; PS: phase shifter.

The output signal of the SD $d(t)$ gives as expected the carrier amplitude A_c [$F_{\rm sd}(0)=1$] and amplitude modulation sidebands, which have been transposed in frequency from $\omega_c \pm \Omega$ to $\pm\Omega$. The phase modulation is not transmitted by the SD.

V. PHASE DEMODULATION: THE PLL

The function of a phase demodulator is to extract the phase $\phi(t)$ from a modulated waveform such as Eq. (12). We discuss here the case of a PLL detector, which is commonly used for FM-DFM. The block diagram presented in Fig. 4 features a linear PLL (see Ref. 26 for PLL classification). A second-order low-pass loop filter was chosen because it gives a behavior that is close to that of our experimental setup.[15] This device includes nonlinear components and thus deserves a special attention.

The sgn function at the input of the PLL [giving an output of +1 (−1) for positive (negative) sign] prevents amplitude noise from perturbing the PLL. This operation is done by a discriminator or a limiter in the electronics.[27] For a small modulation $m_0 \ll 1$, it removes the amplitude dependence of the input signal,

$$\mathrm{sgn}\{A_c[1 + m(t)]\sin[\omega_c t + \phi(t)]\} = \mathrm{sgn}\{\sin[\omega_c t + \phi(t)]\}.$$

The amplitude noise $m(t)$ is eliminated and the phase noise $\phi(t)$ is transmitted.

It can be shown (see Appendix A and Ref. 26) that the PLL of Fig. 4 in its locked state can be modeled as a linear system with a *phase* harmonic function

$$H(\Omega) = \frac{G_{\rm PLL}}{\dfrac{j\Omega}{F_{\rm PLL}(\Omega)} + G_{\rm PLL}}, \quad (16)$$

where the loop gain $G_{\rm PLL}$ has the dimension of an angular frequency and

$$F_{\rm PLL}(\Omega) = \frac{1}{1 + j\Omega\tau_1}\frac{1}{1 + j\Omega\tau_2} \quad (17)$$

is the harmonic function of the second-order low-pass filter. The output of the voltage controlled oscillator (VCO) of the PLL when signal (12) is applied to its input is then given by $e(t)=\cos[\omega_c t + \phi_{\rm out}(t)]$ with

$$\phi_{\rm out}(t) = \frac{2\pi\Delta f(t)}{\Omega} = \frac{\phi_0}{2j}\{H(\Omega)\exp[j(\Omega t + \theta_\phi)] - \overline{H(\Omega)}\exp[-j(\Omega t + \theta_\phi)]\}. \quad (18)$$

Then the excitation signal reads $\mathrm{exc}(t)=\cos[\omega_c t + \phi_{\rm out}(t)$

$+\phi_{PS}]$, where ϕ_{PS} is fixed by the phase shifter (PS) (Fig. 4). In the absence of tip-substrate interaction, $\phi_{PS}=0$ satisfies condition (6). For small phase modulation of amplitude $\phi_0 \ll 2\pi$,

$$\mathrm{exc}(t) \approx \cos(\omega_c t) + \frac{\phi_0}{4}[\exp(j\omega_c t) - \exp(-j\omega_c t)] \times \{H(\Omega)\exp[j(\Omega t + \theta_\phi)] - \text{c.c.}\}, \quad (19)$$

where c.c. stands for the complex conjugate of the first term of the expression in braces.

Here also, the sidebands of the phase modulation at $\omega_c \pm \Omega$ have been transposed to $\pm\Omega$ by the frequency demodulator.

VI. NOISE ANALYSIS OF THE FM-DFM OSCILLATOR

We can now analyze how the noise affects the behavior of the oscillator of Fig. 2.

Two noise sources dominate in FM-DFM:[5,6]

(1) One is the thermal equilibrium noise of the cantilever $\delta F(t)$, which can be modeled by a driving white force noise of two-sided PSD,[3]

$$S_F = 2\gamma k_B T = \frac{2kk_B T}{\omega_0 Q},$$

in $N^2\,Hz^{-1}$, where $k_B T$ is the thermal energy. Due to the equipartition of energy, the power of thermal noise when it is added to a carrier should be equally shared between *amplitude* force noise S_F^a and phase force noise S_F^ϕ without correlation. Thus, $S_F = S_F^a + S_F^\phi$, with $S_F^a = S_F^\phi = \frac{1}{2}S_F$. Note that this noise is *intrinsic* in the sense that it depends only on the cantilever characteristics and not on the deflection measurement method used.

(2) The other is the noise of the deflection sensor $\delta z(t)$, which can be modeled by a white noise of two-sided PSD S_z. As usually, this noise is expressed as an equivalent input noise, which is the noise that has to be applied to the input of an ideal noiseless deflection sensor to produce the measured output noise. It is thus expressed in $m^2\,Hz^{-1}$. In contrast to the thermal noise, the amount and type of noise depend on the specific sensor and electronics used and on its detailed implementation. In the absence of more precise specifications, we will consider a white noise with $S_z^a = S_z^\phi = \frac{1}{2}S_z$. Note that these assumptions are correct for the optical beam deflection method,[18] where the photodiode shot noise is usually dominant, and when using a tuning fork, where the white noise of the transimpedance output amplifier is also dominant.[28]

Other noise sources should be included for a realistic description of any particular FM-DFM setup. Of special importance is the distance noise induced by the vibrations of the mechanical structure and the noise generated by the electronic components of the control system. These contributions will not be considered here. They are too specific to each instrument to lend themselves to a general treatment.

In the AGC block of Fig. 5, the amplitude signal produced by the SD is compared to the constant amplitude set point

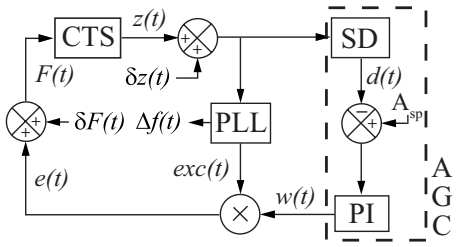

FIG. 5. The thermal noise $\delta F(t)$ and the detection noise $\delta z(t)$ are introduced in the system. CTS represents the cantilever-tip-substrate system.

A_{sp}. The resulting error signal is then shaped by a proportional-integral (PI) corrector.

The signals $z(t)$, $e(t)$, and $F(t)$ are considered as carriers at frequency $\omega_c = \omega_0$, the free resonance frequency of the cantilever in the absence of tip-substrate interaction, amplitude, and phase modulated by sinusoidal components of frequency Ω modeling the noise, as discussed in Sec. III. The amplitude of these components is supposed to be small enough to satisfy the conditions of validity of expressions (14) and (19). The signals $d(t)$, $w(t)$, and $\Delta f(t)$ are demodulated signals at frequency Ω. As a first step, we consider only the thermal force equilibrium noise of PSD S_F.

A. Introduction of the thermal force noise

The thermal noise is modeled as a sinusoidal signal $\delta F(t)$ introduced into the system as shown in Fig. 5. The trajectory $z(t)$ of the tip is given by a general expression of type (13), with $\omega_c = \omega_0$; the free resonance frequency of the cantilever in the absence of tip-substrate interaction

$$z(t) = A_c \sin(\omega_0 t) + \delta z_a\{\sin[(\omega_0 + \Omega)t + \theta_a] + \sin[(\omega_0 - \Omega)t - \theta_a]\} + \delta z_\phi\{\sin[(\omega_0 + \Omega)t + \theta_\phi] - \sin[(\omega_0 - \Omega)t - \theta_\phi]\}, \quad (20)$$

where $\delta z_a = A_c \frac{m_0}{2}$ and $\delta z_\phi = A_c \frac{\phi_0}{2}$. Using expression (14), the dissipation signal at the output of the AGC, taking into account the thermal force noise, can be expressed as

$$w(t) = F_{AGC}(0)(A_c - A_{sp}) + 2\delta z_a\{F_{AGC}(\Omega)\exp[j(\Omega t + \theta_a)] + \text{c.c.}\}, \quad (21)$$

where the harmonic function of the AGC writes

$$F_{AGC}(\Omega) = -F_{sd}(\Omega)\left(P + \frac{I}{j\Omega}\right), \quad (22)$$

P (I) being the gain of the proportional (integral) branch of the PI controller. $F_{AGC}(0)$ diverges to infinity. This divergence can be avoided only if $A_c - A_{sp} = 0$, that is, if $A_c = A_{sp}$. One recovers the well-known action of the integrator gain of a P-I controller, which cancels the amplitude steady-state error. This necessary condition will be maintained in the following of the paper.

The excitation signal at the output of the VCO of the PLL, taking into account the thermal force noise, is given by expression (19), with $\phi_0 = \frac{2\delta z_\phi}{A_{sp}}$,

$$\mathrm{exc}(t) \simeq \cos(\omega_0 t) + \frac{\delta z_\phi}{2A_{\mathrm{sp}}}[\exp(j\omega_0 t) - \exp(-j\omega_0 t)] \times \{H(\Omega)\exp[j(\Omega t + \theta_\phi)] - \mathrm{c.c.}\}. \quad (23)$$

The modulation representing the force thermal noise of PSD S_F is also given by a general expression of type (13), taking into account that the carrier of $F(t)$ is proportional to $\cos(\omega_0 t)$,

$$\delta F(t) = \delta F_a^{(n)}\{\cos[(\omega_0 + \Omega)t + \theta_a^{(n)}] + \cos[(\omega_0 - \Omega)t - \theta_a^{(n)}]\} + \delta F_\phi^{(n)}\{\cos[(\omega_0 + \Omega)t + \theta_\phi^{(n)}] - \cos[(\omega_0 - \Omega)t - \theta_\phi^{(n)}]\}, \quad (24)$$

where $\delta F_a^{(n)}$ and $\theta_a^{(n)}$ ($\delta F_\phi^{(n)}$ and $\theta_\phi^{(n)}$) characterize the amplitude and phase of the thermal force amplitude modulation (phase modulation). $\delta F_a^{(n)}$ ($\delta F_\phi^{(n)}$) is related to S_F^a (S_F^ϕ) by the following relations, as explained in Sec. III A:

$$S_F^a \times 1\ \mathrm{Hz} = \left(\frac{\delta F_a^{(n)}}{2}\right)^2, \quad S_F^\phi \times 1\ \mathrm{Hz} = \left(\frac{\delta F_\phi^{(n)}}{2}\right)^2. \quad (25)$$

Moreover, amplitude noise and phase noise of the excitation force are uncorrelated and considered here as the inputs of the system. The phases at $t=0$ can then be chosen at will without loss of generality. With $\theta_a^{(n)} = \theta_\phi^{(n)} = 0$, expression (24) becomes

$$\delta F(t) = (\delta F_a^{(n)} + \delta F_\phi^{(n)})\cos[(\omega_0 + \Omega)t] + (\delta F_a^{(n)} - \delta F_\phi^{(n)})\cos[(\omega_0 - \Omega)t]. \quad (26)$$

Following Fig. 5, $F(t) = \mathrm{exc}(t)w(t) + \delta F(t)$. Then, for each frequency component $F(\omega)$ of $F(t)$, $Cl(\omega)F(\omega) = z(\omega)$. Neglecting the second-order noise terms—in $\delta z_a \delta z_\phi$—one gets finally the following:

(1) For the frequency ω_0,

$$jCl(\omega_0)F_{\mathrm{AGC}}(0)(A_c - A_{\mathrm{sp}}) = A_{\mathrm{sp}}$$

(remembering that $A_c = A_{\mathrm{sp}}$) and the c.c. of this equation. From expression (1), $jCl(\omega_0) = \frac{Q}{k}$. Then, $F_{\mathrm{AGC}}(0)(A_c - A_{\mathrm{sp}}) = \frac{kA_{\mathrm{sp}}}{Q}$. One recovers condition (5).

(2) For the frequency $\omega_0 + \Omega$,

$$Cl(\omega_0 + \Omega)\left[2F_{\mathrm{AGC}}(\Omega)\widetilde{\delta z_a} + \frac{k}{Q}H(\Omega)\widetilde{\delta z_\phi} + \delta F_a^{(n)} + \delta F_\phi^{(n)}\right] = -j(\widetilde{\delta z_a} + \widetilde{\delta z_\phi}) \quad (27)$$

with $\widetilde{\delta z_a} = \delta z_a \exp(j\theta_a)$ and $\widetilde{\delta z_\phi} = \delta z_\phi \exp(j\theta_\phi)$, and the c.c. of this equation.

(3) For the frequency $\omega_0 - \Omega$,

$$\overline{Cl(\omega_0 - \Omega)}\left[2F_{\mathrm{AGC}}(\Omega)\widetilde{\delta z_a} - \frac{k}{Q}H(\Omega)\widetilde{\delta z_\phi} + \delta F_a^{(n)} - \delta F_\phi^{(n)}\right] = j(\widetilde{\delta z_a} - \widetilde{\delta z_\phi}) \quad (28)$$

and the c.c. of this equation. Using expression (2), one gets $\overline{Cl(\omega_0 - \Omega)} \simeq -Cl(\omega_0 + \Omega)$ and Eq. (28) becomes

$$Cl(\omega_0 + \Omega)\left[2F_{\mathrm{AGC}}(\Omega)\widetilde{\delta z_a} - \frac{k}{Q}H(\Omega)\widetilde{\delta z_\phi} + (\delta F_a^{(n)} - \delta F_\phi^{(n)})\right] = -j(\widetilde{\delta z_a} - \widetilde{\delta z_\phi}). \quad (29)$$

Combining Eqs. (27) and (29), one obtains

$$C(\Omega)[2F_{\mathrm{AGC}}(\Omega)\widetilde{\delta z_a} + \delta F_a^{(n)}] = -j\widetilde{\delta z_a}, \quad (30)$$

$$C(\Omega)\left[\frac{k}{Q}H(\Omega)\widetilde{\delta z_\phi} + \delta F_\phi^{(n)}\right] = -j\widetilde{\delta z_\phi} \quad (31)$$

with $Cl(\omega_0 + \Omega) = C(\Omega)$ [expression (2)]. *These equations* are decoupled in the variables $\widetilde{\delta z_a}$ and $\widetilde{\delta z_\phi}$. *This implies that for noise or small displacements from equilibrium, the two feedback loops of the control system work independently*. It is hardly necessary to insist on the importance of this point, which provides the basis for our subsequent analysis. From these expressions,

$$\widetilde{\delta z_a} = \frac{jC(\Omega)}{1 - jC(\Omega)2F_{\mathrm{AGC}}(\Omega)}\delta F_a^{(n)}, \quad (32)$$

$$\widetilde{\delta z_\phi} = \frac{jC(\Omega)}{1 - j\frac{k}{Q}C(\Omega)H(\Omega)}\delta F_\phi^{(n)}. \quad (33)$$

The dissipation signal can be derived from Eqs. (21) and (32),

$$w(t) = \frac{kA_{\mathrm{sp}}}{Q} + \left[\frac{2jC(\Omega)F_{\mathrm{AGC}}(\Omega)}{1 - 2jC(\Omega)F_{\mathrm{AGC}}(\Omega)}\exp(j\Omega t) + \mathrm{c.c.}\right]\delta F_a^{(n)} = W(0) + \delta W(\Omega)\exp(j\Omega t) + \overline{\delta W(\Omega)}\exp(-j\Omega t), \quad (34)$$

where $w(t)$ has the dimension of a force.

The *mean* power dissipated to excite the cantilever can be calculated from the work performed by the force $F(t)$ on the cantilever,

$$P = \lim_{T\to\infty}\frac{1}{T}\int_0^T F(t)\frac{dz}{dt}dt = \lim_{T\to\infty}\frac{1}{T}W(0)A_{\mathrm{sp}}\omega_0\int_0^T [\cos(\omega_0 t)]^2 dt = \frac{\omega_0 A_{\mathrm{sp}}W(0)}{2}.$$

The *mean* energy dissipated during one period of oscillation reads then

$$P\frac{2\pi}{\omega_0} = \pi A_{\mathrm{sp}}W(0) = \frac{\pi k A_{\mathrm{sp}}^2}{Q}, \quad (35)$$

as shown in Ref. 12. The *instantaneous* dissipated power is then given by $P(t) = \frac{\omega_0 A_{\mathrm{sp}} w(t)}{2}$.

The component at frequency Ω can be extracted from expression (34),

$$\delta W(\Omega) = \frac{2jC(\Omega)F_{\mathrm{AGC}}(\Omega)}{1-2jC(\Omega)F_{\mathrm{AGC}}(\Omega)}\delta F_a^{(n)}. \tag{36}$$

The PSD of w can now be derived using expression (25),

$$\mathrm{PSD}_w(\Omega) = |\delta W(\Omega)|^2 = \left|\frac{2jC(\Omega)F_{\mathrm{AGC}}(\Omega)}{1-2jC(\Omega)F_{\mathrm{AGC}}(\Omega)}\right|^2 4S_F^a.$$

The static limit is easily obtained from the equivalent expression, derived by using relations (2), (15), and (22), with the Laplace variable $s=j\Omega$,

$$\mathrm{PSD}_w(s) = \left|2(Q/k)\frac{Ps+I}{\tau_c\tau_D s^3+(\tau_c+\tau_D)s^2+[1+2(Q/k)P]s+2(Q/k)I}\right|^2 4S_F^a.$$

Then,

$$\lim[\mathrm{PSD}_w(s)]_{s\to 0} = 4S_F^a = \frac{4kk_BT}{\omega_0 Q}. \tag{37}$$

This value agrees with that given in Ref. 8 within a numerical factor on the order of unity and with Ref. 9 within a factor of 2.

From Eq. (18), the frequency detuning is given by

$$\begin{aligned}\Delta f(t) = \frac{\Omega}{2\pi}\phi_{\mathrm{out}}(t) &= \frac{\Omega}{j2\pi A_{\mathrm{sp}}}\{H(\Omega)\exp(j\Omega t)\widetilde{\delta z_\phi} - \mathrm{c.c.}\}\\ &= \Delta f(\Omega)\exp(j\Omega t) + \overline{\Delta f(\Omega)}\exp(-j\Omega t).\end{aligned} \tag{38}$$

With Eq. (33), the component at frequency Ω reads

$$\Delta f(\Omega) = \frac{j\Omega C(\Omega)H(\Omega)}{j2\pi A_{\mathrm{sp}}\left[1-j\frac{k}{Q}C(\Omega)H(\Omega)\right]}\delta F_\phi^{(n)}, \tag{39}$$

leading to

$$\mathrm{PSD}_{\Delta f}(\Omega) = |\Delta f(\Omega)|^2 = \frac{1}{4\pi^2 A_{\mathrm{sp}}^2}\left|\frac{j\Omega C(\Omega)H(\Omega)}{1-j\frac{k}{Q}C(\Omega)H(\Omega)}\right|^2 4S_F^\phi.$$

The static limit is obtained from the equivalent expression using relations (2), (16), and (17),

$$\mathrm{PSD}_{\Delta f}(s) = \frac{s^2}{4\pi^2 A_c^2}\left|\frac{Q}{k}\frac{G_{\mathrm{PLL}}}{\tau_1\tau_2\tau_c s^4+(\tau_1\tau_2+\tau_1\tau_c+\tau_2\tau_c)s^3+(\tau_1+\tau_2+\tau_c)s^2+(1+\tau_c G_{\mathrm{PLL}})s}\right|^2 4S_F^\phi,$$

leading to

$$\lim[\mathrm{PSD}_{\Delta f}(s)]_{s\to 0} = \frac{f_0 k_B T}{2\pi k A_{\mathrm{sp}}^2 Q} \tag{40}$$

giving (in $\mathrm{Hz}^2/\mathrm{Hz}$) the (two-sided) lower limit of thermally induced frequency noise, in agreement with the (one-sided) expression calculated by Albrecht *et al.*[3] and experimentally confirmed in a recent paper.[29] Note that this limit is obtained only when $G_{\mathrm{PLL}} \gg \frac{1}{\tau_c}$, a condition insuring that the thermal noise peak is well within the bandwidth of the PLL, and which is always satisfied for high Q cantilevers in UHV.

B. Introduction of the detection noise

It is straightforward to include in these expressions the modulation representing the *detection noise* $\delta z(t)$, introduced as in expression (26),

$$\begin{aligned}\delta z(t) = &(\delta z_a^{(n)} + \delta z_\phi^{(n)})\sin[(\omega_c+\Omega)t]\\ &+ (\delta z_a^{(n)} - \delta z_\phi^{(n)})\sin[(\omega_c-\Omega)t],\end{aligned}$$

where $\delta z_a^{(n)}$ ($\delta z_\phi^{(n)}$), the amplitude (phase) modulation of the position of the cantilever, is related to the PSD S_z by expressions analogous to Eq. (25).

The calculation proceeds as in Sec. VI A with the new trajectory of the tip given by $z(t)+\delta z(t)$. Equations (30) and (31) become

$$C(\Omega)[2F_{\mathrm{AGC}}(\Omega)(\widetilde{\delta z_a} + \delta z_a^{(n)}) + \delta F_a^{(n)}] = -j\widetilde{\delta z_a}, \tag{41}$$

$$C(\Omega)\left[\frac{k}{Q}H(\Omega)(\widetilde{\delta z_\phi} + \delta z_\phi^{(n)}) + \delta F_\phi^{(n)}\right] = -j\widetilde{\delta z_\phi}, \tag{42}$$

where $\widetilde{\delta z_a}$ ($\widetilde{\delta z_\phi}$) has been replaced by $\widetilde{\delta z_a}+\delta z_a^{(n)}$ ($\widetilde{\delta z_\phi}+\delta z_\phi^{(n)}$) in the left-hand sides. One then gets

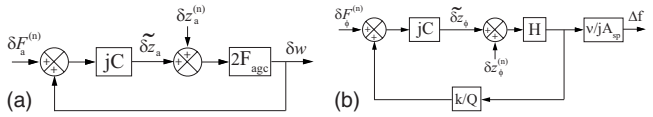

FIG. 6. Block diagrams representing Eqs. (45) and (46). (a) [(b)] illustrates the noise contribution to the dissipation signal δw (frequency detuning signal Δf).

$$\widetilde{\delta z_a} = \frac{jC}{1 - 2jCF_{\mathrm{AGC}}}[\delta F_a^{(n)} + 2F_{\mathrm{AGC}}\delta z_a^{(n)}], \tag{43}$$

$$\widetilde{\delta z_\phi} = \frac{jC}{1 - j\frac{k}{Q}CH}\left[\delta F_\phi^{(n)} + \frac{k}{Q}H\delta z_\phi^{(n)}\right], \tag{44}$$

where the dependencies in Ω have been omitted for simplicity. Equation (43) shows that the amplitude noise of the position of the cantilever couples to the amplitude detection noise and amplitude force thermal noise. Conversely, Eq. (44) shows that the phase noise of the position of the cantilever couples to the phase detection noise and phase force thermal noise.

Expressions (36) and (39) are generalized to

$$\delta W(\Omega) = \frac{2F_{\mathrm{AGC}}}{1 - 2jCF_{\mathrm{AGC}}}[jC\delta F_a^{(n)} + \delta z_a^{(n)}] \tag{45}$$

and

$$\Delta f(\Omega) = \frac{\Omega}{j2\pi A_{\mathrm{sp}}}\frac{H}{1 - j\frac{k}{Q}CH}[jC\delta F_\phi^{(n)} + \delta z_\phi^{(n)}]. \tag{46}$$

Finally, the PSDs with the thermal and detection noise read

$$\mathrm{PSD}_w(\Omega) = 4\left|\frac{2F_{\mathrm{AGC}}}{1 - 2jCF_{\mathrm{AGC}}}\right|^2(|C|^2S_F^a + S_z^a), \tag{47}$$

$$\mathrm{PSD}_{\Delta f}(\Omega) = \frac{\Omega^2}{\pi^2 A_{\mathrm{sp}}^2}\left|\frac{H}{1 - j\frac{k}{Q}CH}\right|^2(|C|^2S_F^\phi + S_z^\phi). \tag{48}$$

The noise propagation in the system can be visualized on the block diagrams of Fig. 6, built from Eqs. (45) and (46). The amplitude demodulation loop of open-loop gain $2jCF_{\mathrm{AGC}}$ involves only amplitude noises, while the frequency demodulation loop of open-loop gain $j\frac{k}{Q}CH$ involves only frequency noises.

The amplitude of the cantilever oscillation[30] is given by $A(t) = A_c[1 + m(t)] = A_{\mathrm{sp}} + 2\delta z_a \cos(\Omega t + \theta_a)$. The PSD of the amplitude can then be evaluated from Eq. (43),

$$\mathrm{PSD}_{\mathrm{amp}}(\Omega) = |\delta z_a|^2 = 4\left|\frac{C}{1 - 2jCF_{\mathrm{AGC}}}\right|^2(S_F^a + 4|F_{\mathrm{AGC}}|^2S_z^a). \tag{49}$$

In the static limit,

$$\lim[\mathrm{PSD}_{\mathrm{amp}}(\Omega)]_{\Omega\to 0} = 4S_z^a. \tag{50}$$

The amplitude PSD is not affected by the force thermal noise in this limit because at low frequency the AGC works ideally: it reacts by adjusting the excitation force $e(t) = w(t)\mathrm{exc}(t)$ to cancel the force thermal noise of the cantilever $\delta F(t)$ (Fig. 5) to maintain its amplitude at the set point value A_{sp}. In contrast, the detection noise, on which the AGC cannot react, is integrally transmitted to the amplitude.

VII. NUMERICAL SIMULATIONS

These analytical expressions rely on a number of approximations. The purpose of the following numerical simulations is to precise their validity domain. The numerical methods and mathematical procedures used to perform the simulations are detailed in Appendix B.

As mentioned previously, S_z, the two-sided PSD of the deflection sensor noise depends on the design of the detection system and varies greatly from one apparatus to the other. To our knowledge, the lowest values for the square root of the one-sided PSD $\sqrt{2S_z}$ obtained with a cantilever beam deflection system are below 10 fm $\mathrm{Hz}^{-1/2}$,[31] while val-

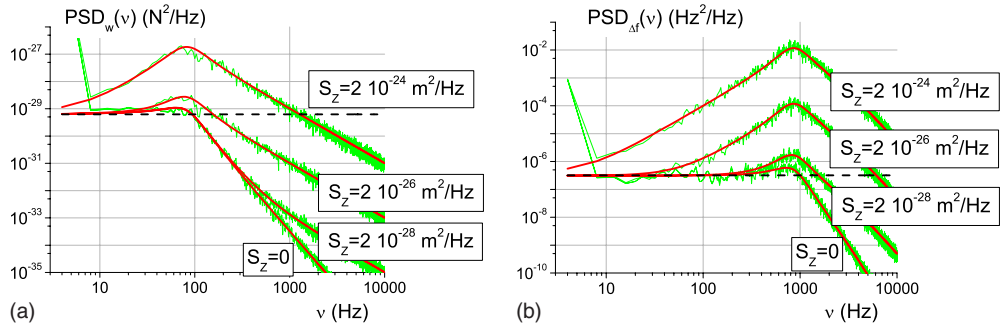

FIG. 7. (Color online) Simulated (in green) and calculated (in red) (a) $\mathrm{PSD}_w(\nu)$ and (b) $\mathrm{PSD}_{\Delta f}(\nu)$ for different amounts of detection noise. Parameters: $f_0 = \frac{\omega_0}{2\pi} = 270$ kHz, $k = 30$ N/m, $Q = 45\,000$, $A_{\mathrm{sp}} = 20$ nm, $P = 0.01$ N m^{-1}, $I = 0.5$ N m^{-1} s^{-1}, $\tau_D = 2$ ms, $G_{\mathrm{PLL}} = 5280$ rad s^{-1}, $\tau_1 = 55$ μs, $\tau_2 = 160$ μs, and $S_F = 3.25 \times 10^{-30}$ N^2 Hz^{-1} ($T = 300$ K). The horizontal dashed lines correspond to the noise thermal limits given by Eqs. (37) and (40).

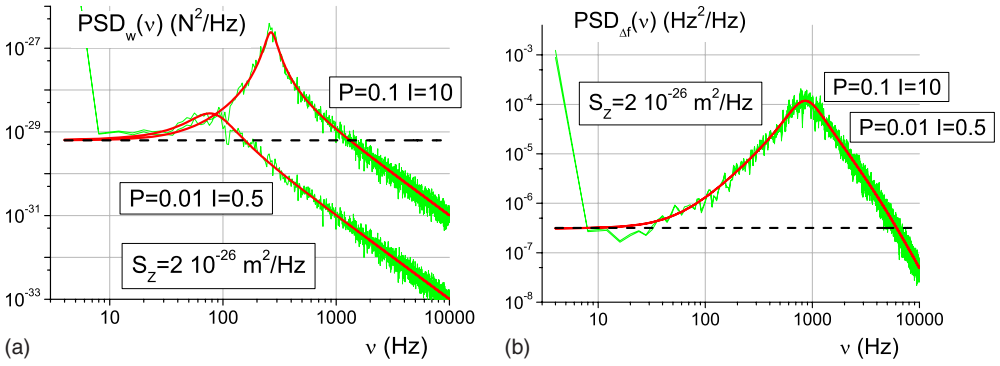

FIG. 8. (Color online) Simulated and calculated (a) $\mathrm{PSD}_w(\nu)$ and (b) $\mathrm{PSD}_{\Delta f}(\nu)$ for $P=0.01$ N m^{-1}, $I=0.5$ N m^{-1} s^{-1} and $P=0.1$ N m^{-1}, $I=10$ N m^{-1} s^{-1}. $S_z=2\times10^{-26}$ m^2 Hz^{-1}.

ues ranging from 100 to 1000 fm Hz$^{-1/2}$ are more typical.

Figure 7 shows $\mathrm{PSD}_w(\nu)$ and $\mathrm{PSD}_{\Delta f}(\nu)$, with $\nu=\Omega/2\pi$, obtained by numerical simulation compared with their analytical expressions (47) and (48) for different amounts of detection noise. The parameters characterizing the cantilever and the different blocks of the AFM machine, taken from Ref. 15, are typical for FM-DFM working in vacuum environment.

The horizontal dashed lines correspond to the noise thermal limits given by Eqs. (37) and (40). When the detection noise is small ($S_z=0$ or $S_z=2\times10^{-28}$ m^2 Hz^{-1}), the spectra are close to their thermal limit in the measuring bandwidth, which is around 100 Hz for the dissipation and 1 kHz from the frequency detuning. In this situation, the variance of the noise, which is given by the integral of the PSD, scales as ν and the standard deviation scales as $\nu^{1/2}$.

The dissipation noise thermal limit is given from expression (37) by $4S_F^a$ when expressed in N^2 Hz^{-1} or $4S_F^a(\pi A_{\mathrm{sp}})^2$ when expressed in (eV/cycle)^2 Hz^{-1} [see expression (35)], giving a value of 10^{-6} (eV/cycle)^2 Hz^{-1} and a variance of 2×10^{-4} (eV/cycle)^2 when integrating from -100 to $+100$ Hz. The dissipation standard deviation is then 14 meV/cycle, comparable to the best experimental data obtained so far.[32]

The frequency detuning noise thermal limit, given by Eq. (40), is 3.3×10^{-7} Hz resulting in a variance of 6.6×10^{-4} Hz^2 when integrating from -1 to $+1$ kHz. The frequency detuning standard deviation is then on the order of 0.026 Hz. When the detection noise dominates [Fig. 7(b) with $S_z=2\times10^{-24}$ m^2 Hz^{-1}], $\mathrm{PSD}_{\Delta f}(\nu)$ increases as ν^2 from 10 Hz to 1 kHz leading to a standard deviation of the noise scaling as $\nu^{3/2}$, an unusual dependence that strongly favors a reduction in the bandwidth to improve the signal-to-noise ratio, as explained by Giessibl.[5]

Figure 8 shows how the setting of the AGC influences $\mathrm{PSD}_w(\nu)$ and $\mathrm{PSD}_{\Delta f}(\nu)$. As expected, $\mathrm{PSD}_{\Delta f}(\nu)$ is not affected by the setting of the AGC since the two closed loops work independently. For $P=0.1$ N m^{-1}, $I=10$ N m^{-1} s^{-1}, a peak appears on $\mathrm{PSD}_w(\nu)$. It corresponds to a tendency of the AGC loop to self-oscillate near the peak frequency. For $P=0.01$ N m^{-1}, $I=0.5$ N m^{-1} s^{-1}, the loop operates near critical damping.

Figure 9 shows the influence of the quality factor Q on $\mathrm{PSD}_w(\nu)$ and $\mathrm{PSD}_{\Delta f}(\nu)$. As expected, the noise on both spectra increases for low values of Q since $S_F\propto Q^{-1}$. It is seen that only the low frequency part of the spectra ($\nu\lesssim300$ Hz) is affected. This is because the thermal noise is attenuated at higher frequency due to the filtering action of the cantilever.

The very good agreement between analytical expressions and simulated spectra shows that the approximations made previously are valid for the considered parameters.

Until now, the cantilever was far from the surface, free from any tip-substrate interaction. In Sec. VIII, we introduce this interaction in the model.

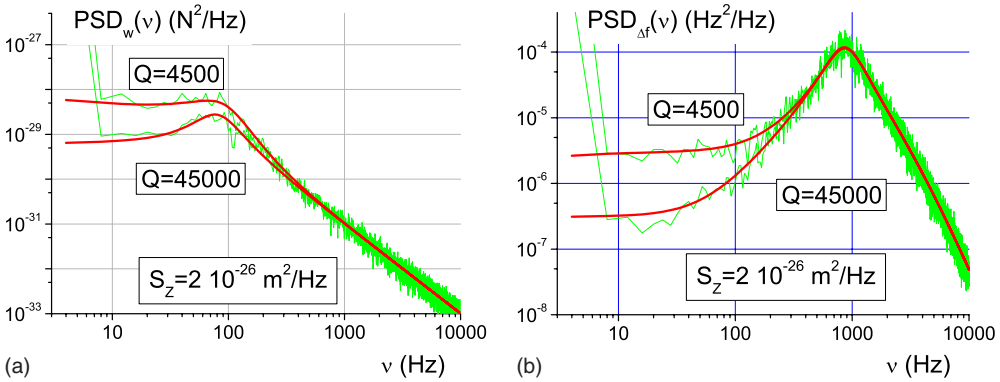

FIG. 9. (Color online) Simulated and calculated (a) $\mathrm{PSD}_w(\nu)$ and (b) $\mathrm{PSD}_{\Delta f}(\nu)$ for $Q=4500$ and $Q=45\,000$. $P=0.01$ N m^{-1}, $I=0.5$ N m^{-1} s^{-1}, and $S_z=2\times10^{-26}$ m^2 Hz^{-1}.

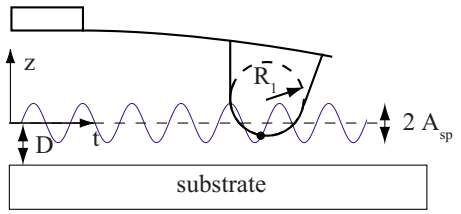

FIG. 10. (Color online) Scheme of the relevant distances for the cantilever-substrate system. z refers to the cantilever displacement and D is the tip-substrate distance when the cantilever is at rest.

VIII. INTRODUCING THE TIP-SUBSTRATE INTERACTION

A. Tip-substrate interaction model

In order to highlight the effects of the tip-surface interaction on the noises of the system, we introduce *conservative* forces. The van der Waals potential for the sphere-plane geometry of the AFM can be modeled by the approximate expression[33,34]

$$U_{\mathrm{vdW}}(D+z) = -\frac{\mathcal{H}R_1}{6(D+z)},$$

where $\mathcal{H}$ is the Hamaker constant of the tip-vacuum-sample junction, R_1 is the tip apex radius, and $D+z$ is the distance between the surface of the sample and the surface of the tip apex (Fig. 10).

The corresponding force is then given by

$$F_{\mathrm{vdW}}(D+z) = -\frac{\partial}{\partial(D+z)}U(D+z) = -\frac{\mathcal{H}R_1}{6(D+z)^2}.$$

This expression was shown to describe van der Waals interaction in a realistic way in several FM-DFM studies.[35–37]

A Morse potential is chosen for the short-range interaction,

$$U_M(D+z) = -E_b\{2\exp[-\kappa(D+z-\sigma)] - \exp[-2\kappa(D+z-\sigma)]\},$$

describing a chemical bond with bonding energy E_b, equilibrium distance σ, and decay length κ^{-1}. The corresponding force is given by

$$F_M(D+z) = 2\kappa E_b\{\exp[-2\kappa(D+z-\sigma)] - \exp[-\kappa(D+z-\sigma)]\}.$$

The total force $F_{\mathrm{int}}=F_{\mathrm{vdW}}+F_M$ (Fig. 11) can be introduced in the system as an additional block as illustrated in Fig. 12, but the nonlinearity in the tip displacement $D+z$ of this new contribution makes the system not suitable for a treatment by ordinary (linear) control theory methods. Linearizing the force around the operating point is suitable only when the oscillation amplitude is small compared to κ^{-1}. The nonlinear block can then be replaced by a simple gain corresponding to the local "stiffness" of the force.

In the opposite limit of large amplitude, as in general for FM-DFM, it can be shown[38,39] that due to the high Q value of the cantilever, which acts as a very narrow band-pass filter

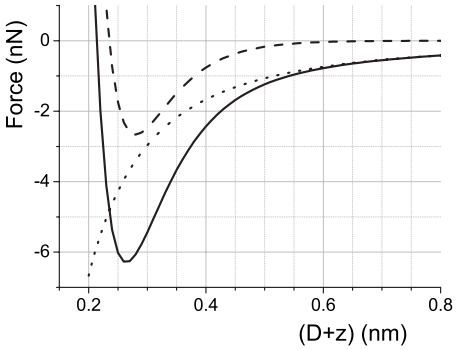

FIG. 11. Continuous line: total force $F_{\mathrm{int}}=F_{\mathrm{vdW}}+F_M$, with $\mathcal{H}=1$ eV, $R_1=10$ nm and the parameters of the Morse potential taken from Ref. 5: $E_b=2.15$ eV, $\sigma=0.235$ nm, and $\kappa=15.5$ nm^{-1}. Dashed line: Morse contribution. Dotted line: van der Waals contribution.

centered at its resonance frequency, and for not too strong nonlinearities, the time Fourier expansions of the tip displacement and of the interaction force can be safely reduced to their fundamental terms: $z(t)\approx A_c\sin(\omega t)$ and $F_{\mathrm{int}}[D+z(t)]\approx F_1\sin(\omega t)\approx\frac{F_1}{A_c}z(t)$ with

$$F_1 = \frac{\omega}{\pi}\int_0^{2\pi/\omega} F_{\mathrm{int}}[D+z(t)]\sin(\omega t)dt. \tag{51}$$

The nonlinear block of Fig. 12(a) can then be replaced by a new block, which is called an equivalent gain, because its transfer function $N(A_c,D)=\frac{F_1}{A_c}$ depends on the values of A_c and $D+z$ at its input but not on the frequency [Fig. 12(b)]. These assumptions and the frame to find the *equivalent gain* of a nonlinear block in a closed-loop system in order to linearize the response are based on the *harmonic equivalent approximation method* detailed in Appendix C. How this method is used to include both conservative and dissipative forces is also presented there. The global harmonic function of the cantilever interacting with the sample is then given by

$$\frac{z(\omega)}{F(\omega)} = \frac{1}{k\left(\frac{\omega_0^2-\omega^2}{\omega_0^2}+\frac{j\omega}{Q\omega_0}\right)-N(A_c,D)}. \tag{52}$$

For $\omega\approx\omega_0$,

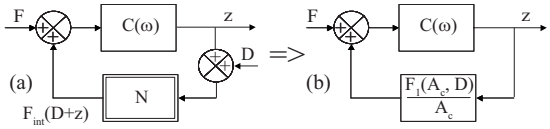

FIG. 12. (a) The tip-substrate force is introduced as a new transfer function N. The double rectangle box underlines the *nonlinear* character of this block. In (b) the block N is replaced by an equivalent gain of transfer function $\frac{F_1}{A_c}$.

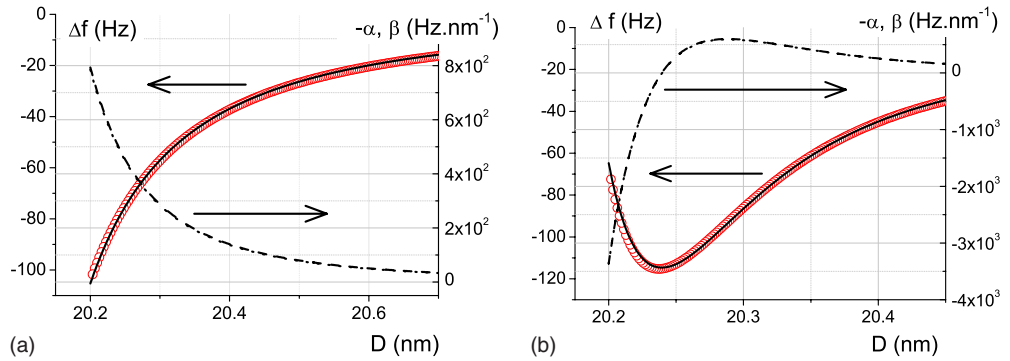

FIG. 13. (Color online) Red circles: $\Delta f(D)=\frac{\Delta\omega(D)}{2\pi}$ obtained with the virtual AFM with the following parameters: $f_0=\frac{\omega_0}{2\pi}=270$ kHz, $k=30$ N m^{-1}, $Q=45\,000$, $A_{sp}=20$ nm, $P=0.1$ N m^{-1}, $I=10$ N m^{-1} s^{-1}, $\tau_D=2$ ms, $G_{PLL}=5280$ rad/s, $\tau_1=55$ μs, $\tau_2=160$ μs, and without noise. Continuous lines: analytical curves from expression (54). Dotted lines: $-\alpha(A_c,D)$ from expression (55). Dashed lines: $\beta(A_c,D)$ from expression (59). $-\alpha$ and β are distinct but not distinguishable at the scale of the figure. (a) van der Waals contribution alone. Tip to sample approach speed: 2 nm/s (b) total (van der Waals+Morse) tip-substrate interaction. Tip to sample approach speed: 1 nm/s.

$$\frac{z(\omega)}{F(\omega)} \approx \frac{1}{k\left(\frac{2(\omega_0-\omega)}{\omega_0}+\frac{j}{Q}\right)-\frac{F_1}{A_c}} = \frac{1}{k\left(\frac{2\left[\omega_0\left(1-\frac{F_1}{2kA_c}\right)-\omega\right]}{\omega_0}+\frac{j}{Q}\right)} \approx \frac{1}{k\left(\frac{2(\omega_r-\omega)}{\omega_r}+\frac{j}{Q}\right)}$$

with the new *renormalized* resonant frequency, $\omega_r=\omega_0(1-\frac{F_1}{2kA_c})$. Then,

$$\frac{\Delta\omega}{\omega_0}=\frac{\omega_r-\omega_0}{\omega_0}=-\frac{F_1}{2kA_c}=-\frac{\omega_0}{2\pi kA_c}\int_0^{2\pi/\omega_0}F_{int}[D+A_c\sin(\omega_0 t)]\sin(\omega_0 t)dt, \tag{53}$$

an expression already derived using the Hamilton-Jacobi approach.[40] Under this approximation, valid only if $\frac{\Delta\omega}{\omega_0}\ll 1$, the transfer function of the cantilever is only affected by this resonance frequency shift. Note that the time scale to establish this relation between $\Delta\omega$ and A_c and D is on the order of one period of the cantilever oscillation, which is a time much shorter than all the other characteristic times of the system. Accordingly, we will consider expression (53) as always valid in the following analysis.

Expression (53) can be evaluated analytically, giving

$$\frac{\Delta\omega}{\omega_0}=-\frac{\mathcal{H}R_1}{6k(D^2-A_c^2)^{3/2}}-2\frac{\kappa E_b}{kA_c}\{\exp[-\kappa(D-\sigma)]J_1(\kappa A_c)-\exp[-2\kappa(D-\sigma)]J_1(2\kappa A_c)\}, \tag{54}$$

where $J_1(x)$ is the Bessel function of the first kind of order 1.[41] This result was derived in Ref. 23 using the variational method developed in Ref. 42.

$\Delta f(D)$ curves obtained using the virtual AFM with the tip-substrate forces displayed in Fig. 11 are compared in Fig. 13 with analytical expression (54). The agreement is excellent even in regions where the force becomes highly nonlinear in the distance D. The contribution of the repulsive part of the Morse potential is responsible for the increase in the frequency shift for small distance in Fig. 13(b).

B. Influence of the tip-substrate interaction on the noises

The frequency shift $\Delta f=\frac{\Delta\omega}{2\pi}$ is given in the case of combined van der Waals and Morse interactions by expression (54). An amplitude fluctuation δA of the oscillation $z(t)$ of the cantilever will then induce a frequency fluctuation

$$\delta\Delta f=\left(\frac{\partial\Delta f}{\partial A}\right)_{A=A_{sp}}\delta A+\mathcal{O}[(\delta A)^2]=\alpha(A_{sp},D)\,\delta A+\mathcal{O}[(\delta A)^2]. \tag{55}$$

The calculated values of $\alpha(A_c=20\text{ nm},D)$, obtained from expression (54), are shown in Fig. 13. This relation shows that, *due to the nonlinear character of the oscillator*, the amplitude noise of $z(t)$ generates frequency noise. This coupling can be taken into account by considering general expression (12) for the position $z(t)$ of the cantilever,

$$z(t)=A_{sp}[1+m(t)]\sin[\omega_c t+\phi(t)]$$

with $m(t)=m_0\cos(\Omega t+\theta_a)$ as previously and $\phi(t)=\phi_0\sin(\Omega t+\theta_\phi)+\phi_A^{int}(t)$, where the new contribution $\phi_A^{int}(t)$ due to amplitude fluctuation reads

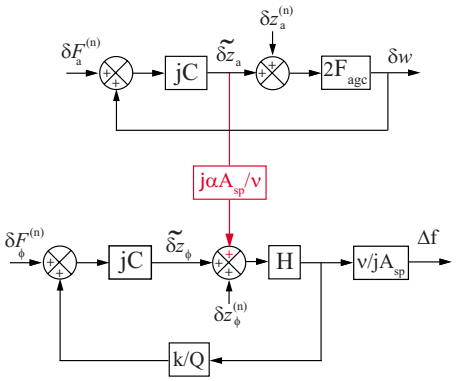

FIG. 14. (Color online) The amplitude noise of the AGC loop is converted into phase noise by the tip-substrate interaction, which is injected into the frequency demodulation loop. The coupling path is in red.

$$\phi_A^{\text{int}}(t) = \frac{\delta\Delta f}{\nu} = \frac{\alpha\delta A}{\nu} = \frac{\alpha}{\nu}A_{\text{sp}}m(t) = \frac{\alpha A_{\text{sp}}m_0}{\nu}\cos(\Omega t + \theta_a).$$

Expression (20) then becomes

$$\begin{aligned} z(t) = {} & A_{\text{sp}}\sin(\omega_c t) + \delta z_a\{\sin[(\omega_c + \Omega)t + \theta_a] \\ & + \sin[(\omega_c - \Omega)t - \theta_a]\} + \delta z_\phi\{\sin[(\omega_c + \Omega)t + \theta_\phi] \\ & - \sin[(\omega_c - \Omega)t - \theta_\phi]\} + \delta z_A^{\text{int}}\left\{\sin\left[(\omega_c + \Omega)t + \theta_a + \frac{\pi}{2}\right]\right. \\ & \left. - \sin\left[(\omega_c - \Omega)t - \theta_a - \frac{\pi}{2}\right]\right\}, \end{aligned}$$

where

$$\delta z_A^{\text{int}} = \frac{\alpha A_{\text{sp}}^2 m_0}{2\nu} = \frac{\alpha A_{\text{sp}}}{\nu}\delta z_a. \tag{56}$$

The new term is, as expected, a phase noise contribution, as defined in Sec. III B 2. Starting from this expression of $z(t)$, the calculation proceeds as in Sec. VI. Expression (45) for $\delta W(\Omega)$ stays unchanged because the phase modulation is not transmitted by the synchronous demodulation of the oscillation amplitude, as demonstrated in Sec. IV and because the tip-surface force is conservative. A nonconservative tip-surface force would be represented by a complex equivalent gain, leading to an increase in the effective Q value of the cantilever, as shown in Appendix C. Expression (46) for $\Delta f(\Omega)$ becomes

$$\Delta f(\Omega) = \frac{\nu}{jA_{\text{sp}}}\frac{H}{1 - j\frac{k}{Q}CH}\left[jC\delta F_\phi^{(n)} + \delta z_\phi^{(n)} + j\frac{\alpha A_{\text{sp}}}{\nu}\widetilde{\delta z_a}\right], \tag{57}$$

where $\widetilde{\delta z_a}$ is still given by expression (43). *The frequency noise generated by the amplitude fluctuations is seen by the phase loop of Fig. 6 as an additional external noise source.* The two loops become coupled, as illustrated in Fig. 14.

Finally,

$$\begin{aligned} \text{PSD}_{\Delta f}(\Omega) = {} & 4\frac{\nu^2}{A_{\text{sp}}^2}\left|\frac{H}{1 - j\frac{k}{Q}CH}\right|^2 \\ & \times\left[|C|^2 S_F^\phi + S_z^\phi + \left(\frac{\alpha A_{\text{sp}}}{\nu}\right)^2\right. \\ & \left.\times\left|\frac{C}{1 - 2jCF_{\text{AGC}}}\right|^2 (S_F^a + 4|F_{\text{AGC}}|^2 S_z^a)\right]. \end{aligned} \tag{58}$$

Due to the conservative interaction between the cantilever and the surface, the four noise sources $(S_F^a, S_F^\phi, S_z^a, S_z^\phi)$ contribute now to the frequency noise.

This expression can be written in a more instructive form from expressions (48) and (49),

$$\text{PSD}_{\Delta f}(\Omega) = \text{PSD}_{\Delta f}^{\text{w.i.}}(\Omega) + \alpha^2\left|\frac{H}{1 - j\frac{k}{Q}CH}\right|^2 \text{PSD}_{\text{amp}}(\Omega),$$

where "w.i." stands for "without interaction."

Simulation results in the presence of the van der Waals interaction alone are shown in Fig. 15. $\text{PSD}_w(\nu)$ is not af-

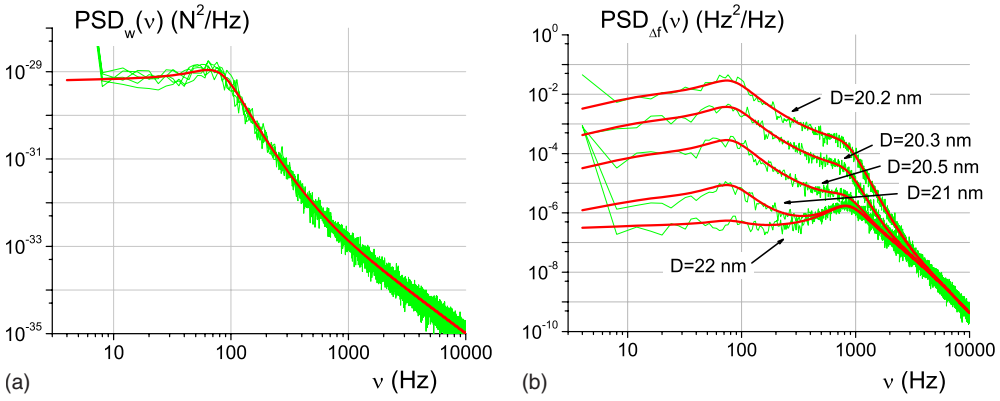

FIG. 15. (Color online) Simulated and calculated (a) $\text{PSD}_w(\nu)$ and (b) $\text{PSD}_{\Delta f}(\nu)$ for the van der Waals contribution alone for different tip-substrate distance D with P=0.01 N m^{-1}, I=0.5 N m^{-1} s^{-1}, $S_F = 3.14\times10^{-30}$ N^2 Hz^{-1} (T=300 K), $S_z = 2\times10^{-28}$ m^2 Hz^{-1}, and the other parameters as in Fig. 13.

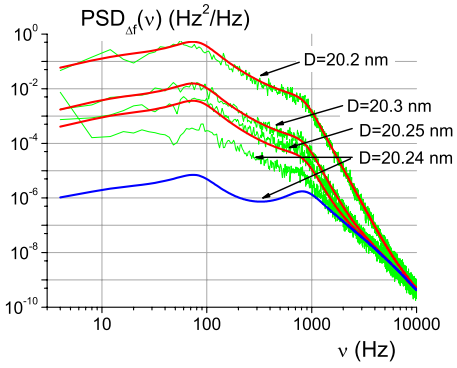

FIG. 16. (Color online) Simulated and calculated $\mathrm{PSD}_{\Delta f}(\nu)$ for the total interaction for different tip-substrate distances D. Same parameters as in Fig. 15. The blue curve is the analytical expression corresponding to $D=20.24$ nm.

fected by the interaction, while $\mathrm{PSD}_{\Delta f}(\nu)$ increases by orders of magnitude when the tip gets closer to the surface due to the term proportional to α^2 in expression (58). The analytical expressions follow closely the simulation results.

When the total interaction (van der Waals+Morse) is introduced, $\mathrm{PSD}_w(\nu)$ (not shown) stays unaffected and $\mathrm{PSD}_{\Delta f}(\nu)$ (Fig. 16) behaves roughly as in the van der Waals case. Nevertheless, two differences appear. First, because of the onset of the repulsive interaction when the tip is closer to the surface, α^2 goes to zero at the minimum of the $\Delta f(D)$ curve ($D \approx 20.24$ nm) shown in Fig. 13(b). This explains why the noise *decreases* from $D=20.3$ nm to $D=20.24$ nm in Fig. 16. Second, the analytical expression does not predict correctly the spectrum at $D=20.24$ nm because α is close to zero at this distance and the expression of the amplitude induced frequency shift (55) can no more be limited to its linear term.

This dependence of the noise on Δf on the distance D can be observed on some of the published experimental $\Delta f(D)$ curves. Figure 2 of the work of Abe *et al.*[43] provides a very clear example of this phenomenon.

IX. CLOSING THE AUTOMATIC DISTANCE CONTROL LOOP

A. Derivation of the distance noise

When used in the constant frequency detuning imaging mode, the control system of the FM-DFM adjusts the tip-substrate distance $D(t)$ in order to maintain the frequency detuning $\Delta f(t)$ equal to the set point Δf_{sp}. This is the role of the automatic distance control (ADC) loop, which is included in the scheme of Fig. 17. The error signal $\Delta f_{\mathrm{sp}} - \Delta f(t)$ is fed into a *P-I* block described by the harmonic function

$$F_{\mathrm{ADC}}(\Omega) = \left(P_{\mathrm{ADC}} + \frac{I_{\mathrm{ADC}}}{j\Omega} \right),$$

and the resulting signal $D(t)$ acts on the tip-substrate distance via a piezoelectric transducer.

Let us consider a modulation of the distance represented by: $\delta D(t) = \delta D_0 \cos(\Omega t + \theta_D)$, where $\Omega \ll \omega_c$ and $\delta D_0 \ll D(t)$.

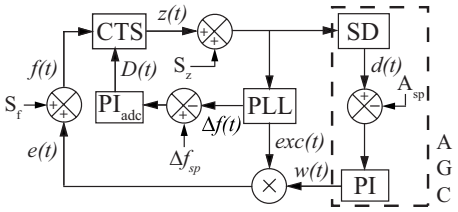

FIG. 17. Scheme of the complete control system, including the ADC.

This low frequency component has no *direct* influence on the behavior of the system because it is very efficiently filtered out by the transfer function of the cantilever. Nevertheless, a distance modulation δD will induce a frequency modulation,

$$\delta\Delta f = \left(\frac{\partial \Delta f}{\partial A} \right)_{A=A_{\mathrm{sp}}} \delta A + \left(\frac{\partial \Delta f}{\partial D} \right)_{A=A_{\mathrm{sp}}} \delta D + \mathcal{O}[(\delta A)^2, (\delta D)^2]$$
$$= \alpha(A_{\mathrm{sp}}, D)\,\delta A + \beta(A_{\mathrm{sp}}, D)\,\delta D + \mathcal{O}[(\delta A)^2, (\delta D)^2]. \quad (59)$$

The calculated values of $\beta(A_c=20\ \mathrm{nm}, D)$, obtained from expression (54), are shown in Fig. 13.

This new contribution results as previously (Sec. VIII B) in a new term in $z(t)$,

$$\begin{aligned} z(t) = {} & z_0 \sin(\omega_c t) + \delta z_a \{\sin[(\omega_c + \Omega)t + \theta_a] \\ & + \sin[(\omega_c - \Omega)t - \theta_a]\} + \delta z_\phi \{\sin[(\omega_c + \Omega)t + \theta_\phi] \\ & - \sin[(\omega_c - \Omega)t - \theta_\phi]\} \\ & + \delta z_A^{\mathrm{int}} \left\{ \sin\left[(\omega_c + \Omega)t + \theta_a + \frac{\pi}{2} \right] \right. \\ & \left. - \sin\left[(\omega_c - \Omega)t - \theta_a - \frac{\pi}{2} \right] \right\} \\ & + \delta z_D^{\mathrm{int}} \left\{ \sin\left[(\omega_c + \Omega)t + \theta_D + \frac{\pi}{2} \right] \right. \\ & \left. - \sin\left[(\omega_c - \Omega)t - \theta_D - \frac{\pi}{2} \right] \right\}, \end{aligned}$$

where $\delta z_A^{\mathrm{int}} = \frac{\alpha A_{\mathrm{sp}}}{\nu} \delta z_a$ and $\delta z_D^{\mathrm{int}} = \frac{\beta A_{\mathrm{sp}}}{2\nu} \delta D_0$.

Equation (42), giving the phase modulation $\widetilde{\delta z_\phi}$, generalizes to

$$C\left[\frac{k}{Q} H(\widetilde{\delta z_\phi} + \delta z_\phi^{(n)} + j\widetilde{\delta z_A^{\mathrm{int}}} + j\widetilde{\delta z_D^{\mathrm{int}}}) + \delta F_\phi^{(n)} \right] = -j\widetilde{\delta z_\phi} \quad (60)$$

with $\widetilde{\delta z_A^{\mathrm{int}}} = \delta z_A^{\mathrm{int}} \exp(j\theta_a)$ and $\widetilde{\delta z_D^{\mathrm{int}}} = \delta z_D^{\mathrm{int}} \exp(j\theta_D)$. But the new contribution $\widetilde{\delta z_D^{\mathrm{int}}}$ cannot be considered as a new noise source, external to the phase loop, because it depends on $\widetilde{\delta z_\phi}$ via the ADC loop. Note that we could also introduce at this level a new *external* source noise to take into account the vibration that could affect the tip-surface distance $D(t)$ due to the vibrations in the environment of the experiment. But as previously mentioned, this type of noise is too specific to lend to a general treatment.

Using

$$\Delta f(t) = \nu\phi_{\text{out}}(t)$$
$$= \frac{\nu}{jA_{\text{sp}}}\{H\exp(j\Omega t)(\widetilde{\delta z_\phi} + \delta z_\phi^{(n)} + j\widetilde{\delta z_A^{\text{int}}} + j\widetilde{\delta z_D^{\text{int}}}) - \text{c.c.}\},$$

the ADC output reads (Fig. 17)

$$\delta D(t) = F_{\text{ADC}}(0)[\Delta f_{\text{sp}} - \Delta f(0)] - \frac{\nu}{jA_{\text{sp}}}[F_{\text{ADC}}H\exp(j\Omega t)(\widetilde{\delta z_\phi} + \delta z_\phi^{(n)} + j\widetilde{\delta z_A^{\text{int}}} + j\widetilde{\delta z_D^{\text{int}}}) - \text{c.c.}]$$

with the component at the frequency Ω,

$$\delta D_0\exp(j\theta_D) = -\frac{2\nu}{jA_{\text{sp}}}F_{\text{ADC}}H(\widetilde{\delta z_\phi} + \delta z_\phi^{(n)} + j\widetilde{\delta z_A^{\text{int}}} + j\widetilde{\delta z_D^{\text{int}}})$$
$$= \widetilde{\delta z_D^{\text{int}}}\frac{2\nu}{\beta A_{\text{sp}}},$$

giving

$$j\widetilde{\delta z_D^{\text{int}}} = -\frac{\beta F_{\text{ADC}}H}{1+\beta F_{\text{ADC}}H}(\widetilde{\delta z_\phi} + \delta z_\phi^{(n)} + j\widetilde{\delta z_A^{\text{int}}}). \quad (61)$$

By replacing $j\widetilde{\delta z_D^{\text{int}}}$ by this expression in Eq. (60), we get

$$\widetilde{\delta z_\phi} = \frac{jC\left[\frac{k}{Q}H(\delta z_\phi^{(n)} + j\widetilde{\delta z_A^{\text{int}}}) + (1+\beta F_{\text{ADC}}H)\delta F_\phi^{(n)}\right]}{1+\beta F_{\text{ADC}}H - jC\frac{k}{Q}H}. \quad (62)$$

$\Delta f(\Omega)$ is then given by the generalization of expression (39),

$$\Delta f(\Omega) = \frac{\nu}{jA_{\text{sp}}}H(\widetilde{\delta z_\phi} + \delta z_\phi^{(n)} + j\widetilde{\delta z_A^{\text{int}}} + j\widetilde{\delta z_D^{\text{int}}})$$
$$= \frac{\nu}{jA_{\text{sp}}}H\frac{\widetilde{\delta z_\phi} + \delta z_\phi^{(n)} + j\widetilde{\delta z_A^{\text{int}}}}{1+\beta F_{\text{ADC}}H}.$$

Using expression (62), we get

$$\Delta f(\Omega) = \frac{\nu}{jA_{\text{sp}}}\frac{H}{1 - j\frac{k}{Q}CH + \beta F_{\text{ADC}}H}$$
$$\times\left[jC\delta F_\phi^{(n)} + \delta z_\phi^{(n)} + j\frac{\alpha A_{\text{sp}}}{\nu}\widetilde{\delta z_a}\right],$$

where $\widetilde{\delta z_a}$ is still given by expression (43).

The PSD reads finally

$$\text{PSD}_{\Delta f}(\Omega) = 4\frac{\nu^2}{A_{\text{sp}}^2}\left|\frac{H}{1 - j\frac{k}{Q}CH + \beta F_{\text{ADC}}H}\right|^2$$
$$\times\left[|C|^2S_F^\phi + S_z^\phi + \left(\frac{\alpha A_{\text{sp}}}{\nu}\right)^2\right.$$
$$\left.\times\left|\frac{C}{1-2jCF_{\text{AGC}}}\right|^2(S_F^a + 4|F_{\text{AGC}}|^2S_z^a)\right]. \quad (63)$$

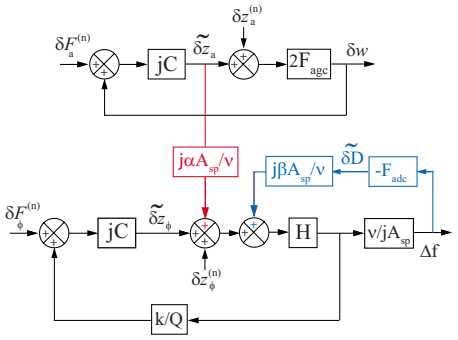

FIG. 18. (Color online) Same as Fig. 14 with the ADC loop (in blue).

This expression can be represented by the block diagram of Fig. 18, which differs from the diagram of Fig. 14 by the addition of the ADC loop, which is isolated in Fig. 19. The closing of the ADC loop changes $\left|\frac{H}{1-j\frac{k}{Q}CH}\right|^2$ in expression (58) to $\left|\frac{H}{1-j\frac{k}{Q}CH+\beta F_{\text{ADC}}H}\right|^2$ in expression (63) because the ADC loop is now connected in parallel with the frequency demodulation loop. The global open-loop gain is then the sum of the open-loop gain of the frequency demodulation loop equal to $j\frac{k}{Q}CH$ and the open-loop gain of the ADC loop equal to $-\beta F_{\text{ADC}}H$ as inferred from the response in distance $\widetilde{\delta D}$ to a distance change δD_{ext} (Fig. 19),

$$\widetilde{\delta D} = \frac{-\beta F_{\text{ADC}}H}{1+\beta F_{\text{ADC}}H}\delta D_{\text{ext}}. \quad (64)$$

The four noise source terms in the brackets of expression (63) are not affected by the closing of the ADC.

Finally, the PSD of the distance D is given by

$$\text{PSD}_D(\Omega) = |F_{\text{ADC}}|^2\text{PSD}_{\Delta f}(\Omega) \quad (65)$$

or

$$\text{PSD}_D(\Omega) = \frac{4}{\beta^2}\frac{\nu^2}{A_{\text{sp}}^2}\left|\frac{\beta F_{\text{ADC}}H}{1 - j\frac{k}{Q}CH + \beta F_{\text{ADC}}H}\right|^2$$
$$\times\left[|C|^2S_F^\phi + S_z^\phi + \left(\frac{\alpha A_{\text{sp}}}{\nu}\right)^2\right.$$
$$\left.\times\left|\frac{C}{1-2jCF_{\text{AGC}}}\right|^2(S_F^a + 4|F_{\text{AGC}}|^2S_z^a)\right]. \quad (66)$$

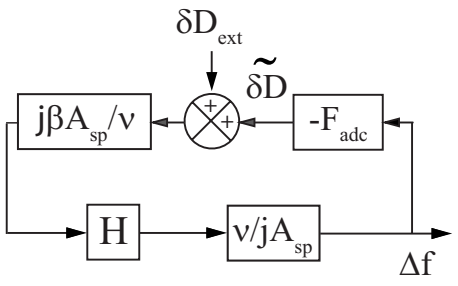

FIG. 19. Block diagram of the ADC loop.

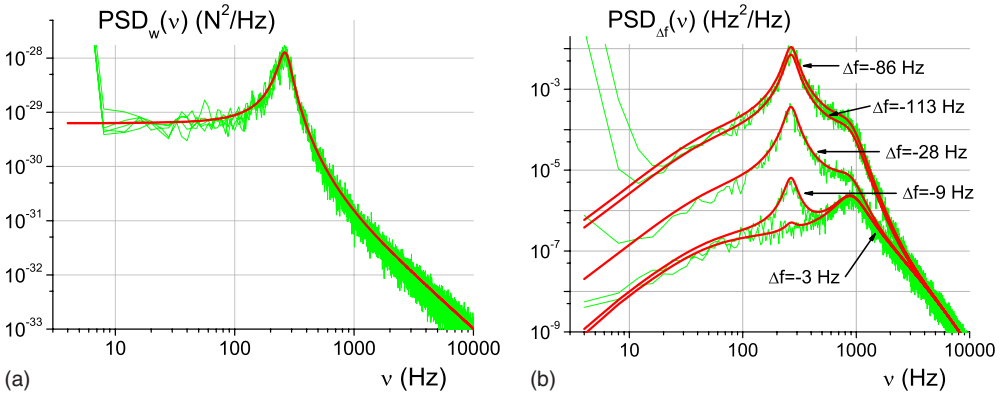

FIG. 20. (Color online) Simulated and calculated (a) $\mathrm{PSD}_w(\nu)$ and (b) $\mathrm{PSD}_{\Delta f}(\nu)$ for the total tip-substrate interaction for different Δf_{sp} with $P=0.1$ N m^{-1}, $I=10$ N m^{-1} s^{-1}, $S_F=3.14\times10^{-30}$ N^2 Hz^{-1} ($T=300$ K), $S_z=2\times10^{-28}$ m^2 Hz^{-1}, and the other parameters as in Fig. 13. βF_{ADC} is kept constant ($\beta P_{\mathrm{ADC}}=0.2$ and $\beta I_{\mathrm{ADC}}=400$ s^{-1}).

Numerical results of Fig. 20 show that, as expected, $\mathrm{PSD}_w(\nu)$ is not affected by the closing of the ADC loop, while $\mathrm{PSD}_{\Delta f}(\nu)$ is well described by expression (63). Note the correspondence between the frequency shifts labeling the spectra of Fig. 20(b) and the distances labeling the spectra of Fig. 16(b). They are related by the $\Delta f(D)$ curve of Fig. 13(b). The $\mathrm{PSD}_{\Delta f}(\nu)$ spectrum that would correspond to $D=20.2$ nm in Fig. 16(b) does not appear in Fig. 20(b) because β becomes negative for this distance, corresponding to a negative slope of the $\Delta f(D)$ curve: the ADC loop becomes unstable in these conditions.

Figure 21 compares $\mathrm{PSD}_{\Delta f}(\nu)$ and $\mathrm{PSD}_D(\nu)$ spectra for two different settings of the ADC feedback loop. In Figs. 21(a) and 21(b), βF_{ADC} is kept constant in order to fix the same D measuring bandwidth for all spectra [expression (64)]. The optimal bandwidth is fixed by the scanning speed chosen for imaging and by the topography of the surface under consideration. It is then normal to keep it at a constant value while varying the frequency detuning set point. In these conditions, it is seen in Fig. 21(b) that the distance noise globally decreases as the tip gets closer to the surface. This phenomenon originates in the β^{-2} dependence of $\mathrm{PSD}_D(\nu)$ observed in expression (66) for constant βF_{ADC}. In contrast, F_{ADC} is kept constant in Figs. 21(c) and 21(d). Now,

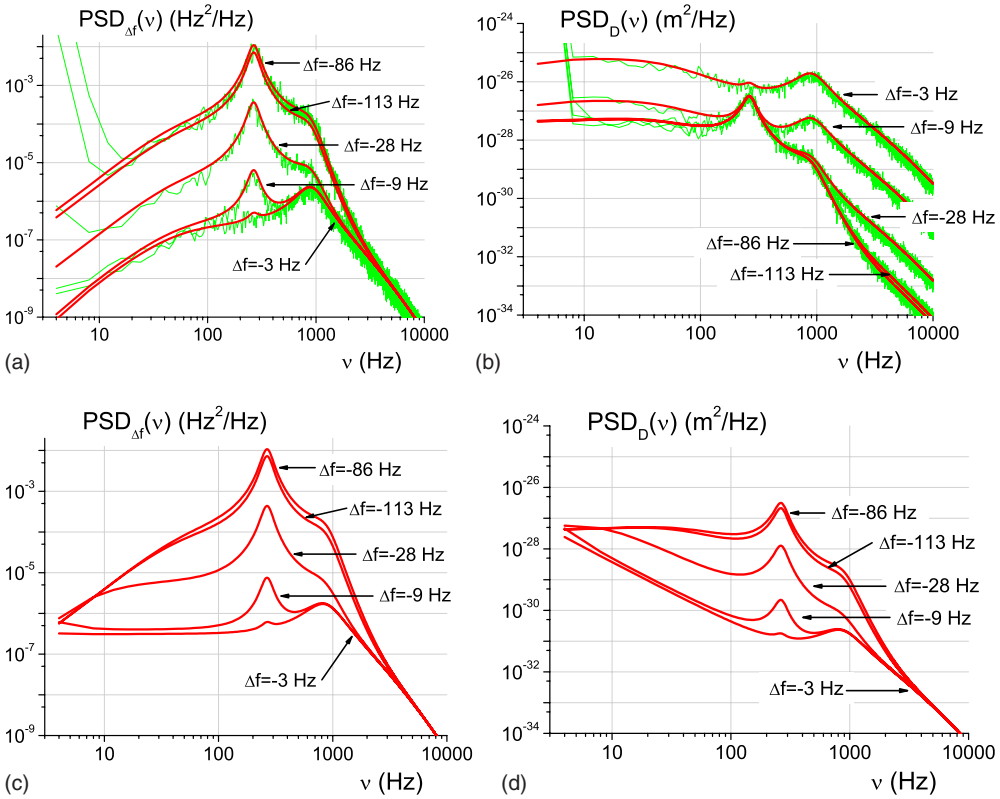

FIG. 21. (Color online) [(a) and (c)] $\mathrm{PSD}_{\Delta f}(\nu)$; [(b) and (d)] $\mathrm{PSD}_D(\nu)$. For (a) and (b), $\beta P_{\mathrm{ADC}}=0.2$ and $\beta I_{\mathrm{ADC}}=400$ s^{-1}. For (c) and (d) $P_{\mathrm{ADC}}=3.5\times10^{-13}$ m s, $I_{\mathrm{ADC}}=7\times10^{-10}$ m. Otherwise, same parameters as for Fig. 20.

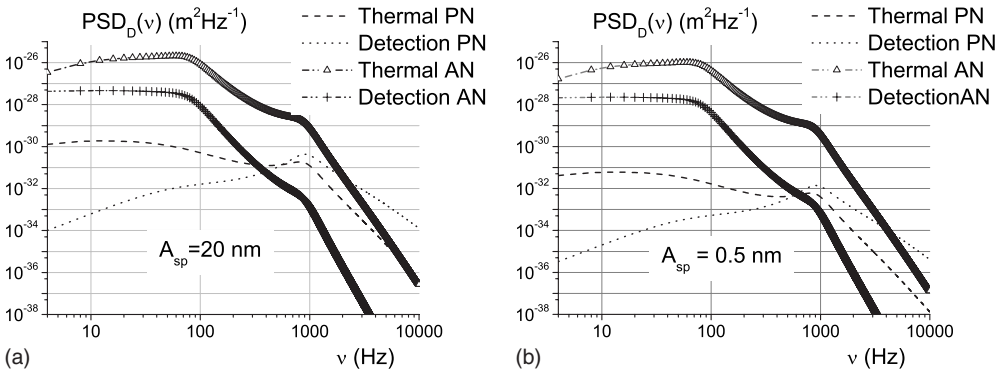

FIG. 22. $\mathrm{PSD}_D(\nu)$ decomposed in its four contributions for (a) $A_{\mathrm{sp}}=20$ nm and (b) $A_{\mathrm{sp}}=0.5$ nm. $P=0.01$ N m^{-1}, $I=0.5$ N m^{-1} s^{-1}, $\beta P_{\mathrm{ADC}}=0.2$, $\beta I_{\mathrm{ADC}}=400$ s^{-1}, $S_F=3.14\times10^{-30}$ N^2 Hz^{-1}, and $S_z=2\times10^{-28}$ m^2 Hz^{-1}.

the distance noise behaves as the frequency noise: it increases as the tip gets closer to the surface. Nevertheless, this setting of the ADC loop is not realistic as it leads to very small bandwidth when the tip is far from the surface. This is the reason why no simulation data are presented in Figs. 21(c) and 21(d); the calculation time to stabilize the tip-substrate distance becomes very long for small frequency set point Δf_{sp} with this ADC setting. This behavior is well known to experimentalists, who are used to reduce the ADC bandwidth when decreasing Δf_{sp} (tip closer to the surface) to avoid instabilities.

B. Influence of the amplitude set point on the distance noise

The amplitude set point is one of the important settings accessible to the experimentalist and its influence on the distance noise has been analyzed in detail by Giessibl *et al.*[5,44] To discuss this point, we rewrite expression (66) in the following form:

$$\mathrm{PSD}_D(\Omega) = \frac{4}{\beta^2}\frac{\nu^2}{A_{\mathrm{sp}}^2}\left|\frac{\beta F_{\mathrm{ADC}}H}{1-j\frac{k}{Q}CH+\beta F_{\mathrm{ADC}}H}\right|^2(|C|^2S_F^{\phi}+S_z^{\phi}) + \left(\frac{\alpha}{\beta}\right)^2\left|\frac{\beta F_{\mathrm{ADC}}H}{1-j\frac{k}{Q}CH+\beta F_{\mathrm{ADC}}H}\right|^2\mathrm{PSD}_{\mathrm{amp}}(\Omega) = \mathrm{PN}+\mathrm{AN}.$$

Two contributions can be distinguished in this expression:

(i) The first one originates from the phase noise sources, S_F^{ϕ} and S_z^{ϕ}, which induce distance fluctuations via the conversion factor β^{-1}. This is the starting point of the analysis carried on by Giessibl *et al.*[44] to evaluate the optimal imaging parameters for FM-DFM. If, as previously, βF_{ADC} is kept constant to fix the D measuring bandwidth, the amplitude dependence of this phase noise (PN) contribution follows $(\beta A_{\mathrm{sp}})^{-2}$.

(ii) The second one originates from the amplitude noise sources, as a direct consequence of the coupling of the two feedback loops illustrated in Figs. 14 and 18: S_F^a and S_z^a induce frequency fluctuations via the conversion factor α and then distance fluctuations via the conversion factor β^{-1}. As demonstrated in the following, this contribution, which was not considered until now, cannot generally be neglected. The amplitude dependence of this amplitude noise (AN) contribution follows $(\alpha/\beta)^2$.

$\mathrm{PSD}_D(\nu)$ is decomposed in its four terms in Fig. 22 for large ($A_{\mathrm{sp}}=20$ nm [Fig. 22(a)]) and small ($A_{\mathrm{sp}}=0.5$ nm [Fig. 22(b)]) amplitudes and for the same closest tip-substrate distance $b=D-A_{\mathrm{sp}}=0.35$ nm. It is seen that the AN contribution (triangles and crosses) dominates the distance noise spectrum in both cases.

This behavior can be understood from the way α and β depend on A_{sp}. As demonstrated in Ref. 44 and confirmed in Fig. 23, β scales approximately as $A_{\mathrm{sp}}^{-3/2}$ when the amplitude is larger than the range of the interaction, given here by $\kappa^{-1}\approx0.065$ nm. Then the PN noise contribution decreases as $(\beta A_{\mathrm{sp}})^{-2}\sim A_{\mathrm{sp}}$, as observed in Fig. 22. This observation constitutes the main argument developed in Ref. 44. But in the same time, $(\alpha/\beta)^2$ decrease from unity for large amplitude to 0.49 for $A_{\mathrm{sp}}=0.5$ nm. The AN contribution is then hardly reduced because the decrease in the noise due to the increase in β is approximately compensated by the increase in $-\alpha$ (Fig. 23). Somewhat unexpectedly, the relative contribution of the nonlinear terms increases for small amplitudes.

This observation shows that *reducing the amplitude does not lead to a significant reduction in the distance noise* at least in the amplitude range explored in this analysis.

Of course, reducing the amplitude to $A_{\mathrm{sp}}=0.5$ nm while keeping the cantilever stiffness at $k=30$ N/m is not practical in most situations because kA_{sp} should stay above a threshold

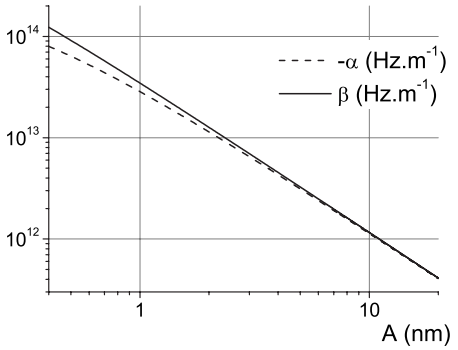

FIG. 23. $-\alpha(A_{\mathrm{sp}},A_{\mathrm{sp}}+0.35$ nm) and $\beta(A_{\mathrm{sp}},A_{\mathrm{sp}}+0.35$ nm).

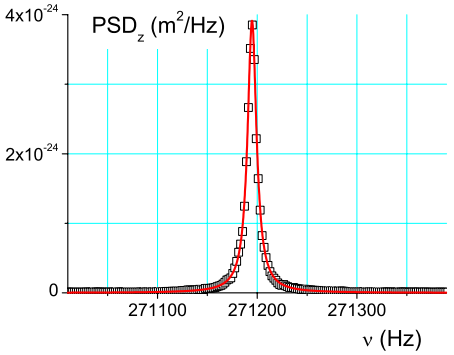

FIG. 24. (Color online) Two-sided PSD of the thermal fluctuations of the cantilever at room temperature. Open black squares: average of 256 experimental spectra. Red line: analytical expression (67).

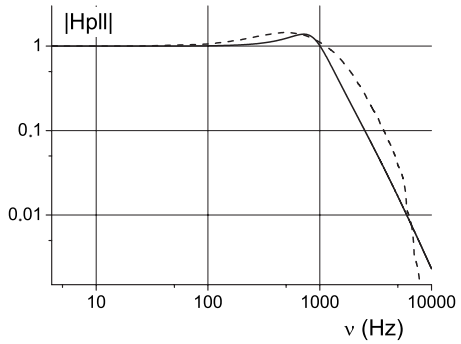

FIG. 26. Modulus of $H(\nu)$ used to perform the numerical simulations of previous sections (continuous line) and experimentally determined (dashed line).

value to avoid "jump-to-contact" instabilities. The amplitude and the stiffness should be optimized simultaneously. This important discussion is outside the scope of this work and will be the subject of a forthcoming paper.

X. COMPARISON WITH EXPERIMENT

We present some experimental measurements to show how they compare to the analytical formula derived previously. A more precise study will be published elsewhere. The experiments were performed with a room temperature AFM/scanning tunneling microscopy (STM) from Omicron Nanotechnology,[45] where a Superlum laser diode was used instead of the original light source.[46] The control system from Omicron (with the SCALA software)[45] was used in conjunction with the amplitude controller and the easy PLL demodulator commercialized by NanoSurf,[19] configured in the PLL-excitation mode.

The nanosensor NCH cantilever[47] was characterized by measuring the PSD of its fluctuations at room temperature and adjusting this spectrum with

$$\mathrm{PSD}_z(\nu) = |Cl(\nu)|^2 S_F + S_z. \tag{67}$$

As demonstrated in Fig. 24, a good fit is obtained with $f_0 = 271\,195$ kHz, $k = 30$ N/m, $Q = 25\,000$ and $S_z = 8 \times 10^{-27}$ m^2 Hz^{-1}.

Figure 25 shows $\mathrm{PSD}_w(\nu)$ and $\mathrm{PSD}_{\Delta f}(\nu)$ obtained in the constant frequency detuning mode while investigating the surface of a cleaved KBr monocrystal in UHV (Ref. 46) for two values of the frequency shift, with an amplitude setup of $A_{\mathrm{sp}} = 4$ nm. A good agreement can be reached with the parameters indicated in the legend and with the following two modifications:

(1) It was necessary to use the experimentally determined transfer function of the PLL instead of expression (16) derived from our model PLL to get a better agreement (see Fig. 26).

(2) Not surprisingly, it was necessary to introduce noise in the distance D of PSD $S_D = 10^{-26}$ m^2 Hz^{-1}. This noise is probably generated by the high voltage amplifier that controls the tip-substrate distance piezoceramics.

As expected, we confirm the main conclusions of the previous calculations and simulations. $\mathrm{PSD}_w(\nu)$ does not depend on the frequency shift, while $\mathrm{PSD}_{\Delta f}(\nu)$ increases when $|\Delta f|$ increases, i.e., when the tip gets closer to the surface. The peaks that appear near 200 Hz in the Δf spectra of Fig. 25(b) are the signature of the nonlinear tip-substrate interaction, which injects amplitude noise in the frequency demodulation loop.

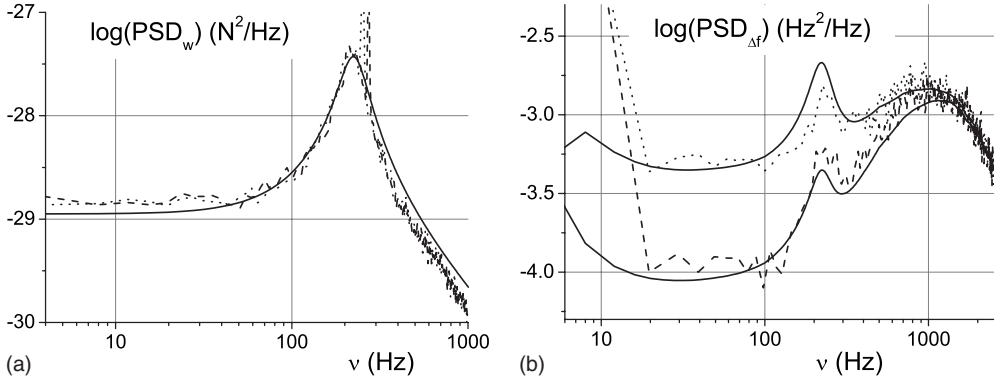

FIG. 25. (a) $\mathrm{PSD}_w(\nu)$ and (b) $\mathrm{PSD}_{\Delta f}(\nu)$ for $\Delta f_{\mathrm{sp}} = -10$ Hz (dashed lines) and $\Delta f_{\mathrm{sp}} = -28$ Hz (dotted lines). The continuous line in (a) is analytical expression (47); the continuous lines in (b) correspond to analytical expression (63) with $\beta = -\alpha = 35$ and 85 Hz nm^{-1}). Other parameters: $P = 0.07$ N m^{-1}, $I = 1$ N m^{-1} s^{-1}, $\tau_D = 2$ ms, $P_{\mathrm{ADC}} = 2 \times 10^{-13}$ m s, and $I_{\mathrm{ADC}} = 4 \times 10^{-10}$ m.

XI. DISCUSSION AND CONCLUSION

The model FM-DFM on which are based the calculations and simulations presented in this work does not include all the devices that constitute the real experiment. It is minimal in the sense that all the nonessential elements have been eliminated for the sake of simplicity and generality. Despite this simplification, it is still adequate to reproduce experimental measurements, as shown by the comparison presented in Sec. X.

The methods developed here can be adapted to different FM-DFM setups without difficulty. For instance, it is quite easy to obtain analytical expressions for the different noises when the so-called "self-excitation" mode is used instead of the PLL-excitation mode, which was chosen in this work. It is also straightforward to include specific elements such as a band-pass filter at the input of the PLL as reported by many groups in order to increase the signal-to-noise ratio of the frequency demodulator.

The comparisons that were systematically performed between the analytical predictions and the numerical simulations demonstrate that the approximations that were proposed are essentially correct for calculating the noise of the instrument. An exception has been reported for the data of Fig. 16(b) where the linear approximation of expression (55) breaks down. More generally, these analytical expressions cannot be used to address situations where high level signals are involved, for instance, in the presence of very high noise or transient signals resulting from abrupt changes in the state of the instrument, such as when scanning a very rough surface at high speed. Nevertheless, they can be used to calculate the response to small excitations such as a step in the distance D or in the energy dissipated between the tip and the surface. As such, they are useful to rationalize the settings of the feedback loops of the AFM control system, which are usually chosen on an empirical basis. This will be done in a future paper.

The main results and consequences of this work are the following:

(i) Distinguishing carefully between amplitude and phase noise leads to a description of the way noises affect the behavior of the instrument in terms of two feedback loops (Fig. 6); the AGC loop carries amplitude noise, while the frequency demodulation loop carries phase noise.

(ii) These loops are independent when the tip is far from the surface of the sample; they become coupled when the tip-substrate interaction is taken into account (Figs. 14 and 18). The magnitude of these couplings is determined by two coefficients that are related to the nonlinear character of the cantilever oscillation induced by the interaction: $\alpha(A_{\mathrm{sp}},D)=\left(\frac{\partial\Delta f(A,D)}{\partial A}\right)_{A=A_{\mathrm{sp}}}$ and $\beta(A_{\mathrm{sp}},D)=\left(\frac{\partial\Delta f(A,D)}{\partial D}\right)_{A=A_{\mathrm{sp}}}$.

(iii) If the tip-substrate interaction is *conservative*, which is the case considered so far, these couplings generate only extra noise terms, which affect the frequency shift $\Delta f(t)$, but not the dissipation signal $w(t)$.

(iv) A *dissipative* interaction can be easily incorporated in the model. If this interaction has a stochastic component, which is generally the case,[48] it will generate noise that will appear on *both* the dissipation signal $w(t)$ and the frequency shift $\Delta f(t)$ signal.

(v) The noise in the frequency detuning $\Delta f(t)$ [expression (63)] and in the distance $D(t)$ [expression (66)] depends on the frequency detuning set point Δf_{sp} via two contributions: (1) a change in the measuring tip-surface distance bandwidth, determined by β, and (2) the noise coming from the AGC loop, determined by α. The role of the nonlinear contribution to these noises had not been considered before this work.

Among the possible applications of the methods developed here are the following:

(i) Choosing the best experimental strategy for a given type of measurement constitutes certainly a major issue to which the present work can contribute. An example of special importance is how to optimize the parameters of the oscillating probe (resonance frequency, stiffness, amplitude), which was already discussed by Giessibl *et al.*[44] This work was done without considering the nonlinear contributions to the noise. A preliminary evaluation, using our analytical expressions, shows that even in the case of a tuning fork working at rather low amplitude,[49] the neglect of the nonlinear terms can lead to significant quantitative disagreements.

(ii) As already mentioned, the analytical expressions we derived give transfer functions that can be used to rationalize the feedback loop settings of the instrument. The usual methods of control theory can then be applied for this purpose.

Finally, we believe that understanding and mastering a scientific instrument does not reduce to an understanding of its functioning principles but that it requires also getting a detailed view on the way noise affects its behavior. We hope that this work will contribute to a better understanding of FM-DFM.

ACKNOWLEDGMENTS

This work was financially supported by the French ANR PNANO-2005 DiNaMo project. M.A.V.C. acknowledges financial support from Consejo de Ciencia y Tecnologia del estado de Aguascalientes (CONCYTEA) (see Ref. 50).

APPENDIX A: DERIVATION OF THE PHASE TRANSFER FUNCTION OF THE PHASE-LOCKED LOOP DEMODULATOR

1. Voltage controlled oscillator

The voltage controlled oscillator (VCO) is the key component of the PLL (Fig. 4). It oscillates at an angular frequency ω_{VCO} related to the input signal $d(t)$ by

$$\omega_{\mathrm{VCO}}(t)=\omega_{\mathrm{CF}}+K_0 d(t), \tag{A1}$$

where ω_{CF} and K_0 are the VCO central frequency and gain. In FM-DFM, the central frequency ω_{CF} is usually fixed by the user at ω_0, the free resonance frequency of the cantilever: $\omega_{\mathrm{CF}}=\omega_0$.

The VCO produces a sinusoidal signal $e(t)$ whose phase is given by integrating $\omega_{\mathrm{VCO}}(t)$,

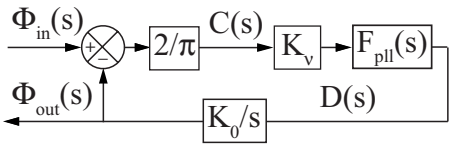

FIG. 27. Block diagram of the PLL for signal phases.

$$e(t) = \cos\left\{\int_0^t [\omega_0 + K_0 d(t')]dt'\right\} = \cos[\omega_0 t + \phi_{\text{out}}(t)] \tag{A2}$$

with

$$\phi_{\text{out}}(t) = K_0 \int_0^t d(t')dt'. \tag{A3}$$

2. Phase transfer function of the PLL demodulator

An amplitude and phase modulated signal is applied to the input of the frequency demodulator (Fig. 4),

$$a(t) = A_c[1 + m(t)]\sin[\omega_c t + \phi_{\text{in}}(t)].$$

As discussed in Sec. V, the signal is passed through a sgn block. If $m(t) \ll 1$,

$$b(t) = \text{sgn}[a(t)] = \text{sgn}\{\sin[\omega_c t + \phi_{\text{in}}(t)]\}.$$

This expression can be expanded in Fourier series,

$$b(t) = \frac{4}{\pi}\sin[\omega_c t + \phi_{\text{in}}(t)] + (\text{odd harmonics}). \tag{A4}$$

When the PLL is locked, $\omega_{\text{VCO}} = \omega_c$. The difference between the frequency of the input signal $\omega_c = \omega_{\text{VCO}}$ and the resonance frequency of the cantilever far from the surface $\omega_0 = \omega_{\text{CF}}$ is then given by expression (A1): $\Delta\omega = \omega_{\text{VCO}} - \omega_{\text{CF}} = K_0 d(t)$ and the VCO generates a sinusoidal signal $e(t) = \cos[\omega_c t + \phi_{\text{out}}(t)]$. Then,

$$c(t) \approx \frac{4}{\pi}\sin[\omega_c t + \phi_{\text{in}}(t)]\cos[\omega_c t + \phi_{\text{out}}(t)]$$

$$\approx \frac{2}{\pi}\sin[\phi_{\text{in}}(t) - \phi_{\text{out}}(t)],$$

where the higher harmonics, which will be attenuated by the following low-pass filter, have been neglected. If the phase error $\phi_{\text{in}}(t) - \phi_{\text{out}}(t) \ll 2\pi$ rad,

$$c(t) \approx \frac{2}{\pi}[\phi_{\text{in}}(t) - \phi_{\text{out}}(t)], \tag{A5}$$

The multiplier plays the role of a *phase comparator*. Then,

$$d(t) \approx \frac{2K_v}{\pi}[\phi_{\text{in}}(t) - \phi_{\text{out}}(t)]. \tag{A6}$$

From the diagram of Fig. 27, the open-loop phase transfer function is given in Laplace form by

$$H_{\text{OL}}(s) = \frac{\Phi_{\text{out}}(s)}{\Phi_{\text{in}}(s)} = \frac{2}{\pi}K_v F_{\text{PLL}}(s)\frac{K_0}{s}, \tag{A7}$$

where the Laplace transforms are represented by capital letters and $F_{\text{PLL}}(s)$ is the transfer function of the low-pass filter, considering the Laplace transforms of expressions (A3) and (A5). The close-loop transfer function reads then

$$H_{\text{CL}}(s) = \frac{\Phi_{\text{out}}(s)}{\Phi_{\text{in}}(s)} = \frac{G_{\text{PLL}}}{\dfrac{s}{F_{\text{PLL}}(s)} + G_{\text{PLL}}} \tag{A8}$$

with the equivalent gain $G_{\text{PLL}} = \frac{2}{\pi}K_v K_0$, also named the natural pulsation of the PLL.[26]

APPENDIX B: METHODS AND PROCEDURES FOR THE NUMERICAL SIMULATIONS

Methods

Numerical simulations were performed with our virtual AFM (Ref. 15) using the MATLAB Simulink toolbox.[14] The AGC is modeled as in Figs. 3 and 5 and the PLL is modeled as in Fig. 4. Care was taken to wait a long enough time after the start of the simulation to avoid transients contributing to the spectra. The variable time-step solver ode45 of MATLAB, which is based on an explicit Runge-Kutta (4,5) formula, the Dormand-Prince pair was used with a maximum step size of 10^{-7} s. A simulation time of 0.25 s per spectrum was chosen, giving a frequency bin of 4 Hz. In the following, we establish the relation between continuous and discrete spectral quantities to precise the conventions used.

a. Fourier transforms: Relation between the continuous and discretized spectrum

An analog signal $x(t)$ is discretized,

$$x_i = x[t = (i-1)\delta t], \quad i = 1, \ldots, N,$$

where $T = (N-1)\delta t$ is the duration of the sample. The (continuous) Fourier transform (FT) is defined as

$$X(f) \equiv \int_{-\infty}^{+\infty} x(t)\exp(-j2\pi ft)dt. \tag{B1}$$

The discretized values of the FT reads

$$G_k = X[f = (k-1)\delta f], \quad k = 1, \ldots, N$$

with $\delta f = \frac{1}{(N-1)\delta t} = \frac{1}{T}$ is the frequency bin. Here,

$$G_k = \int_{-\infty}^{+\infty} x(t)\exp\left[-j2\pi\frac{(k-1)t}{(N-1)\delta t}\right]dt$$

$$\simeq \sum_{i=1}^{N} x_i \exp\left[-j2\pi\frac{(k-1)(i-1)}{(N-1)}\right]\delta t.$$

Then, $G_k \simeq \delta t X_k$, where X_k is the discrete Fourier transform (DFT) of $\{x_i\}$. To recover the FT value from the discrete transform, one should multiply by δt (this is consistent with dimensional analysis).

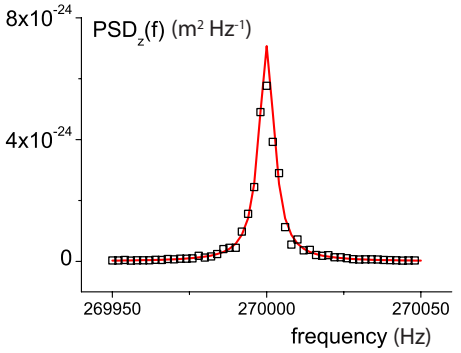

FIG. 28. (Color online) PSD of z for a cantilever submitted to a random thermal force (see text). Squares: simulation data; red line: analytical expression: $\mathrm{PSD}_z(f)=|Cl(f)|^2 S_F$. $T=0.5$ s, $\delta t=10^{-7}$ s. 30 spectra have been averaged.

b. Expression of the power spectral density

In the following and unless otherwise specified, we use *two-sided* power spectral density given by $S_X(f) \equiv \lim_{T\to\infty} \frac{|X(f)|^2}{T}$.[51] Its discrete expression is given by

$$\frac{|X_k|^2 \delta t^2}{T} = \delta t \frac{|X_k|^2}{(N-1)}. \tag{B2}$$

The variance of $x(t)$ is related to its PSD by

$$\langle x^2 \rangle = \frac{1}{T}\int_0^T |x(t)|^2 dt = \int_{-\infty}^{\infty} \frac{|X(f)|^2}{T} df = \int_{-\infty}^{\infty} S_X(f) df. \tag{B3}$$

The discrete expression of $\int_{-\infty}^{\infty} S_X(f) df$ is

$$\langle x^2 \rangle = \int_{-\infty}^{\infty} S_X(f) df \simeq \sum_{k=1}^{N} \frac{|X_k|^2 \delta t^2}{T} \frac{1}{T} = \frac{\delta t^2}{T^2} \sum_{k=1}^{N} |X_k|^2. \tag{B4}$$

PSDs were calculated from the modulus square of the Fourier transform of the data after application of a Hanning window using expression (B2). Variances can be obtained from the spectra by expression (B4).

These considerations can be illustrated by the result of the simulation shown in Fig. 28. A random force of two-sided PSD $S_F=\frac{2kk_BT}{\omega_0 Q}$, corresponding to the equilibrium thermal noise, is applied to a cantilever with $f_0=\frac{\omega_0}{2\pi}=270$ kHz, $k=30$ N/m, and $Q=45\,000$ at room temperature ($k_BT=4\times10^{-21}$ J). The PSD of the cantilever displacement z is shown for positive frequencies in Fig. 28. The variance of z is obtained by expression (B4) from twice the area under the resonance peak (to take into account the negative frequencies) with $\langle z^2 \rangle = 1.25\times10^{-22}$ m^2 Hz^{-1}. This value is in good agreement with the value given by the equipartition of energy $\langle z^2 \rangle = \frac{k_BT}{k} = 1.33\times10^{-22}$ m^2 Hz^{-1}.

APPENDIX C: THE HARMONIC EQUIVALENT APPROXIMATION METHOD

For a linear system with input w and output s, one defines the transfer function starting from sinusoidal test functions of the type $w(t)=w_0 \sin(\omega t)$ by the amplitude ratio $\rho=\frac{s_0}{w_0}$ and the phase Φ of the response $s(t)=s_0 \sin(\omega t+\Phi)$. Thanks to the properties of linearity, ρ and Φ are functions of the frequency of the input, but they do not depend on its amplitude: this makes possible to define a transfer function that is related to ω only.

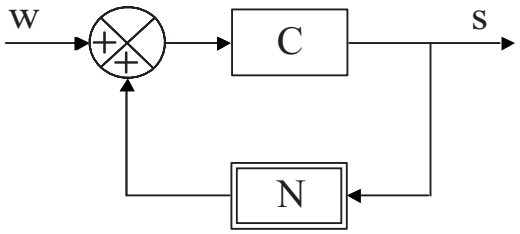

FIG. 29. Closed loop nonlinear system with the linear transfer function C and the equivalent transfer function N providing the nonlinear signal $nl(t)$.

In order to extend this procedure to a nonlinear system, one is led to study the output for a harmonic input $w(t)=w_0 \sin(\omega t)$. The response will be in general periodic but nonsinusoidal. If by an arbitrary convention, one defines at the output of the nonlinear element N (see Fig. 29) a sinusoidal function

$$nl(t) = nl_1 \sin(\omega t + \Upsilon) = a_1 \sin(\omega t) + a_1' \cos(\omega t) \tag{C1}$$

declared (arbitrarily) equivalent to the input $s(t)$, one can define for the system an *equivalent transfer function* or *generalized transfer function* with

$$\text{modulus} = \frac{nl_1}{s_1} \quad \text{and} \quad \text{argument} = \Upsilon.$$

As the equivalent sinusoidal function one generally takes the first harmonic of $s(t)$. The difference with the linear case is twofold:

(i) There is an arbitrary element in the choice of the equivalent sinusoid as the output.

(ii) The *equivalent transfer function* obtained depends not only on ω but also on the input amplitude s_1 since there is no more proportionality of the effects to the causes as in the linear case,

$$N(s_1,\omega) = \frac{nl_1}{s_1} e^{j\Upsilon} \quad \text{and} \quad \Upsilon = \Upsilon(s_1,\omega) \tag{C2}$$

with

$$nl_1 e^{j\Upsilon} = a_1 + j a_1'. \tag{C3}$$

The concept of stability of a system can thus change according not only to its frequency of operation but also to the amplitude of the signal entering the transfer function.

If the equivalent transfer function depends only on ω, one will then speak about a *pseudolinear system*.[52] If the equivalent transfer function depends only on s_1, one will speak then about *equivalent gain* $N(s_1)$.[22]

It is generally difficult to specify precisely the validity

domain of this method and one has to rely on analytical calculations or numerical simulations to check it. In the particular case where the linear block C that follows the nonlinear body presents a marked resonance peak, the approximation is justified. The nonlinear block becomes in this case *quasilinear*.

Note that this method is a special case of the method of describing functions,[53] which was used once in the context of tapping-mode AFM.[54]

1. Conservative interaction case

Let us consider for this study the van der Waals tip-surface force, as defined in Sec. VIII A,

$$nl(t) = -\frac{\mathcal{H}R_1}{6[D + s(t)]^2}, \tag{C4}$$

where D is supposed to be constant. This relation between $s(t)$ and $nl(t)$ corresponds to the block N of Fig. 29.

From this relation, let us obtain the equivalent gain $N(s_1)$ knowing that $nl(t)=a_1 \sin(\omega t)+a_1' \cos(\omega t)$ [see relation (C1)] in the harmonic equivalent approximation. From this relation,

$$a_1 = \frac{\omega}{\pi}\int_0^{2\pi/\omega} nl(t)\sin(\omega t)dt \tag{C5}$$

and

$$a_1' = \frac{\omega}{\pi}\int_0^{2\pi/\omega} nl(t)\cos(\omega t)dt. \tag{C6}$$

Replacing $nl(t)$ by relation (C4) we get $a_1=\frac{\mathcal{H}R}{3}\frac{s_1}{(D^2-s_1^2)^{3/2}}$ and $a_1'=0$. Using Eqs. (C1) and (C2), we obtain

$$N(s_1) = \frac{\mathcal{H}R}{3}\frac{1}{(D^2 - s_1^2)^{3/2}}. \tag{C7}$$

The equivalent transfer function depends only on s_1; it is thus an equivalent gain. It is purely *real*, characterizing a *conservative* interaction. To find the harmonic function of the cantilever oscillating in interaction with surface, one uses this expression of the equivalent gain in relation (52) such that

$$\frac{s_1}{w_0}(\omega) = \frac{1}{k}\frac{1}{\left(1 - \frac{\omega^2}{\omega_0^2}\right) + j\frac{\omega}{Q\omega_0} - \frac{\mathcal{H}R}{3k}\frac{1}{(D^2 - s_1^2)^{3/2}}}. \tag{C8}$$

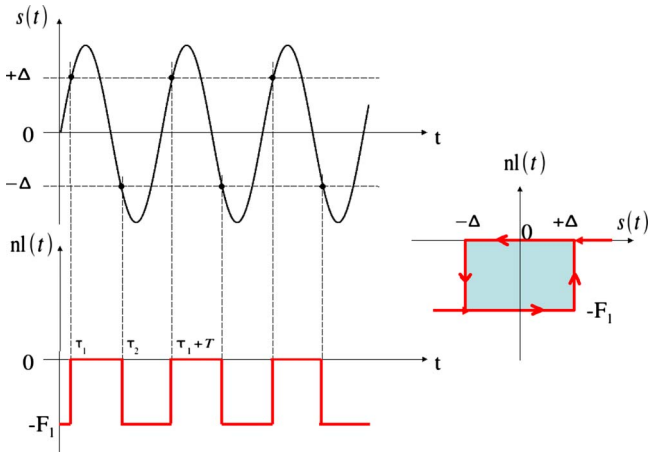

FIG. 30. (Color online) Model for a dissipative interaction.

2. Dissipative interaction case

To illustrate how a nonconservative interaction can be treated in a similar way, we propose the simple model of Fig. 30, which is built is such a way that the force when the tip gets closer to the surface is different from the force when the tip retracts, generating the force hysteresis cycle shown in the figure. In such a situation an energy given by the area of the hysteresis cycle $\mathcal{A}=2F_1\Delta$ is dissipated during each cycle, in addition to the energy required to maintain the cantilever amplitude at s_1, given by $\pi\frac{k}{Q}s_1^2$.

As previously, the expression of the equivalent gain $N(s_1)$ can be established by using relations (C5) and (C6),

$$a_1 = \frac{\omega}{\pi}\int_0^{\tau_1}(-)F_1 \sin(\omega t)dt + \frac{\omega}{\pi}\int_{\tau_2}^{2\pi/\omega}(-)F_1 \sin(\omega t)dt$$

$$= \frac{2F_1}{\pi}\sqrt{1 - \left(\frac{\Delta}{s_1}\right)^2}$$

and

$$a_1' = \frac{\omega}{\pi}\int_0^{\tau_1}(-)F_1 \cos(\omega t)dt + \frac{\omega}{\pi}\int_{\tau_2}^{2\pi/\omega}(-)F_1 \cos(\omega t)dt$$

$$= -\frac{2F_1}{\pi}\frac{\Delta}{s_1}.$$

Thus a *complex* equivalent gain is obtained,

$$N(s_1) = \frac{a_1 + ja_1'}{s_1} = \frac{2F_1}{\pi s_1}\left(\sqrt{1 - \left(\frac{\Delta}{s_1}\right)^2} - j\frac{\Delta}{s_1}\right), \tag{C9}$$

and the harmonic function characterizing the cantilever in interaction reads

$$\frac{s_1}{w_0}(\omega) = \frac{1}{k}\frac{1}{\left[\left(1 - \frac{\omega^2}{\omega_0^2}\right) - \frac{2F_1}{\pi k s_1}\sqrt{1 - \left(\frac{\Delta}{s_1}\right)^2}\right] + j\frac{\omega}{Q\omega_0}\left[1 + \frac{Q\omega_0}{\omega}\frac{2F_1}{\pi k}\frac{\Delta}{s_1^2}\right]}. \tag{C10}$$

The comparison with expression (C8) shows that the imaginary part of the equivalent gain leads to a reduction in the effective quality factor of the system. This is the direct consequence of the dissipative character of the interaction and one can easily generalize this observation to any dissipative interaction.

Let us introduce the dimensionless quantity $\Xi = 1 + \frac{Q\omega_0}{\omega}\frac{2F_1}{\pi k}\frac{\Delta}{s_1^2}$, which gives the effective quality factor $\frac{Q}{\Xi}$ in the presence of dissipative interaction. Ξ is related to the ratio of $\mathcal{A}=2F_1\Delta$, the energy dissipated by the nonconservative interaction, and to $\pi\frac{k}{Q}s_1^2$, the energy dissipated in the absence of interaction to maintain the cantilever amplitude at s_1. We also introduce the other dimensionless quantity $\Psi = \frac{2F_1}{\pi k s_1}\sqrt{1-(\frac{\Delta}{s_1})^2}$, which is the ratio of the stiffness of the conservative interaction force to the cantilever stiffness k. The generalized harmonic function of the oscillator reads then

$$\frac{s_1}{w_0}(\omega) = \frac{1}{k}\frac{1}{\left[\left(1-\frac{\omega^2}{\omega_0^2}\right)-\Psi\right]+j\frac{\omega}{Q\omega_0}\Xi}. \quad \text{(C11)}$$

3. General case for conservative and dissipative interactions

The expressions of Ψ and Ξ can be generalized to an arbitrary force $F[s(t),D]$,

$$\Psi = \frac{\omega}{s_1\pi k}\int_0^{2\pi/\omega} F[s(t),D]\sin(\omega t)dt = \frac{a_1}{s_1 k}, \quad \text{(C12)}$$

$$\Xi = 1 + \frac{Q\omega_0}{s_1\pi k}\int_0^{2\pi/\omega} F[s(t),D]\cos(\omega t)dt = 1 + \frac{a_1'}{s_1 k}\frac{Q\omega_0}{\omega}. \quad \text{(C13)}$$

Ψ and Ξ are two dimensionless quantities associated with the conservative and the dissipative contributions of the tip-sample interaction averaged over one oscillation period, respectively. The expression for Ψ was originally derived by Giessibl[40] using the Hamilton-Jacobi formalism. A similar expression for Ξ was obtained by Sader *et al.*[55]

*gauthier@cemes.fr

[1] Nanotechnology **18** (2007), special issue. selected papers form NCAFM 2996: The 9th International Conference on Non-Contact Atomic Force Microscopy, Kobe, Japan, 16–20 July 2006, edited by M. Tomitori and H. Onishi.

[2] T. Fukuma, M. J. Higgins, and S. P. Jarvis, Phys. Rev. Lett. **98**, 106101 (2007).

[3] T. R. Albrecht, P. Grütter, D. Horne, and D. Rugar, J. Appl. Phys. **69**, 668 (1991).

[4] U. Dürig, H. R. Steinauer, and N. Blanc, J. Appl. Phys. **82**, 3641 (1997).

[5] F. J. Giessibl, Rev. Mod. Phys. **75**, 949 (2003).

[6] T. Fukuma, M. Kimura, K. Kobayashi, K. Matsushige, and H. Yamada, Rev. Sci. Instrum. **76**, 053704 (2005).

[7] J. Polesel-Maris and S. Gauthier, J. Phys.: Conf. Ser. **61**, 949 (2007).

[8] W. Denk and D. W. Pohl, Appl. Phys. Lett. **59**, 2171 (1991).

[9] P. Grütter, Y. Liu, P. Leblanc, and U. Dürig, Appl. Phys. Lett. **71**, 279 (1997).

[10] P. F. Cohadon, A. Heidmann, and M. Pinard, Phys. Rev. Lett. **83**, 3174 (1999).

[11] T. Corbitt, C. Wipf, T. Bodiya, D. Ottaway, D. Sigg, N. Smith, S. Whitcomb, and N. Mavalvala, Phys. Rev. Lett. **99**, 160801 (2007).

[12] J. P. Cleveland, B. Anczykowski, A. E. Schmid, and V. B. Elings, Appl. Phys. Lett. **72**, 2613 (1998).

[13] J. P. Aimé, R. Boisgard, L. Nony, and G. Couturier, Phys. Rev. Lett. **82**, 3388 (1999).

[14] MATLAB 6.5 with Simulink, The MathWorks, Inc. (http://www.mathworks.com/).

[15] J. Polesel-Maris and S. Gauthier, J. Appl. Phys. **97**, 044902 (2005).

[16] T. Trevethan, L. Kantorovich, J. Polesel-Maris, S. Gauthier, and A. Shluger, Phys. Rev. B **76**, 085414 (2007).

[17] J. E. Sader and S. P. Jarvis, Phys. Rev. B **74**, 195424 (2006).

[18] G. Meyer and N. M. Amer, Appl. Phys. Lett. **53**, 1045 (1988).

[19] NanoSurf AG, Grammetstrasse 14, CH-4410 Liestal (http://www.nanosurf.com/).

[20] W. P. Robins, *Phase Noise in Signal Sources*, IEE Telecommunications Series 9, edited by J. E. Flood and C. J. Hughes (Peregrinus, London, 1982).

[21] A. N. Cleland and M. L. Roukes, J. Appl. Phys. **92**, 2758 (2002).

[22] J. Ch. Gille, M. J. Pelegrin, and P. Decaulne, *Feedback Control Systems* (McGraw-Hill, New York, 1959).

[23] L. Nony, A. Baratoff, D. Schär, O. Pfeiffer, A. Wetzel, and E. Meyer, Phys. Rev. B **74**, 235439 (2006).

[24] G. Couturier, J. P. Aimé, J. Salardenne, and R. Boisgard, Eur. Phys. J.: Appl. Phys. **15**, 141 (2001).

[25] M. Gauthier, R. Pérez, T. Arai, M. Tomitori, and M. Tsukada, Phys. Rev. Lett. **89**, 146104 (2002).

[26] R. E. Best, *Phase-Locked Loops: Design, Simulation and Applications* (McGraw-Hill, New York, 1999).

[27] K. Kobayashi, H. Yamada, H. Itoh, T. Horiuchi, and K. Matsushige, Rev. Sci. Instrum. **72**, 4383 (2001).

[28] R. D. Grober, J. Asimovic, J. Schuck, D. Hessman, P. J. Kindlemann, J. Hespanha, A. S. Morse, K. Karrai, I. Tiemann, and S. Manus, Rev. Sci. Instrum. **71**, 2776 (2000).

[29] S. Rast, U. Gysin, and E. Meyer, Phys. Rev. B **79**, 054106 (2009).

[30] Note that this is the real amplitude of the oscillation, not the amplitude $d(t)$ at the output of the amplitude demodulator.

[31] T. Fukuma and S. Jarvis, Rev. Sci. Instrum. **77**, 043701 (2006).

[32] M. Guggisberg, M. Bammerlin, A. Baratoff, R. Lüthi, Ch. Loppacher, M. Battiston, J. Lü, R. Bennewitz, E. Meyer, and H.-J. Güntherodt, Surf. Sci. **461**, 255 (2000).

[33] J. Israelachvili, *Intermolecular and Surface Forces* (Academic, New York, 1992).

[34] C. Argento and R. H. French, J. Appl. Phys. **80**, 6081 (1996).

[35] M. Guggisberg, M. Bammerlin, Ch. Loppacher, O. Pfeiffer, A. Abdurixit, V. Barwich, R. Bennewitz, A. Baratoff, E. Meyer, and H.-J. Güntherodt, Phys. Rev. B **61**, 11151 (2000).
[36] M. A. Lantz, H. J. Hug, R. Hoffmann, P. J. A. van Schendel, P. Kappenberger, S. Martin, A. Baratoff, and H.-J. Güntherodt, Science **291**, 2580 (2001).
[37] J. Polesel-Maris, A. Piednoir, T. Zambelli, X. Bouju, and S. Gauthier, Nanotechnology **14**, 1036 (2003).
[38] J. Polesel-Maris, Ph.D. thesis, University of Toulouse III, 2005 (http://tel.archives-ouvertes.fr/tel-00009666/fr/).
[39] G. Couturier, R. Boisgard, D. Dietzel, and J. P. Aimé, Nanotechnology **16**, 1346 (2005).
[40] F. J. Giessibl, Phys. Rev. B **56**, 16010 (1997).
[41] M. Abramowitz and I. Stegun, *Handbook of Mathematical Functions* (Dover, New York, 1970).
[42] L. Nony, R. Boisgard, and J.-P. Aimé, Eur. Phys. J. B **24**, 221 (2001).
[43] M. Abe, Y. Sugimoto, O. Custance, and S. Morita, Appl. Phys. Lett. **87**, 173503 (2005).
[44] F. J. Giessibl, H. Bielefeld, S. Hembacher, and J. Mannhart, Appl. Surf. Sci. **140**, 352 (1999).
[45] Omicron Nanotechnology GmbH, Limburger Strasse 75, D-65232 Taunusstein (http://www.omicron.de/).
[46] M. A. Venegas de la Cerda, J. Abad, A. Madgavkar, D. Martrou, and S. Gauthier, Nanotechnology **19**, 045503 (2008).
[47] Nanosensors, Rue Jaquet-Droz 1, Case Postale 216, CH-2002 Neuchatel (http://www.nanosensors.com/).
[48] L. N. Kantorovich and T. Trevethan, Phys. Rev. Lett. **93**, 236102 (2004).
[49] F. J. Giessibl, S. Hembacher, M. Herz, Ch. Schiller, and J. Mannhart, Nanotechnology **15**, S79 (2004).
[50] http://aguascalientes.gob.mx/concytea/
[51] A. Papoulis, *Signal Analysis* (McGraw-Hill, New York, 1977).
[52] A. Fossard, A. Piedplat, and M. Gauvrit, L'Onde Electrique **XLIV**, 909 (1964).
[53] A. Gelb and W. E. Van der Velde, *Multiple-Input Describing Functions and Nonlinear System Design* (McGraw-Hill, New York, 1968).
[54] A. Sebastian, M. V. Salapaka, D. J. Chen, and J. P. Cleveland, J. Appl. Phys. **89**, 6473 (2001).
[55] J. E. Sader, T. Uchihashi, M. J. Higgins, A. Farrell, Y. Nakayama, and S. Jarvis, Nanotechnology **16**, S94 (2005).